Hindawi
International Journal of Energy Research
Volume 2024, Article ID 5510119, 21 pages
https://doi.org/10.1155/2024/5510119

WILEY | Hindawi

Research Article

Unsteady Mixed Convection Flows in a Rectangular Duct and Dynamical Behaviors of Flow Channel Insert

Zhi-Hong Liu [1,2] **Jie Wang,** [1] **Ming-Jiu Ni,** [1] **and Nian-Mei Zhang** [1]

[1] *School of Engineering Science, University of Chinese Academy of Sciences, Beijing, China 100190*
[2] *Center for Ultimate Energy, ShanghaiTech University, Shanghai, China 201210*

Correspondence should be addressed to Nian-Mei Zhang; nmzhang@ucas.ac.cn

Received 11 July 2023; Revised 29 January 2024; Accepted 20 February 2024; Published 11 March 2024

Academic Editor: Amin Shokrollahi

Buoyancy-assisted upward MHD flows and dynamical behaviors of flow channel insert (FCI) in the dual-coolant lead-lithium (DCLL) blanket are studied numerically. Based on our internally developed and validated solver, the dynamical behaviors of magneto-thermo-fluid-structure coupled multiphysical field are investigated. A large amplitude, low frequency, and quasiperiodic unsteady reverse flow at high Re (31000), high Gr (3.5×10^{11}), and moderate magnetic field (0.7~1.7T) is found in the DCLL blanket. This intricate phenomenon has been discovered for the first time, representing a combination of separate experimental results from Melnikov et al. (2016) and Khanal and Lei (2012). In our study of this large amplitude, low frequency, and quasiperiodic unsteady reverse flows, the importance of the cold helium gas to the instability of fluid flow in the bulk region and the thermal conductivity of the FCI to convection structure and instability are first found and recognized. Additionally, we take into account the effects of the temperature field and flow field on structural deformation and mechanical behavior of FCI, and we have discovered several intriguing phenomena, such as (1) the stability of fluid flow in the bulk region depends on the strength of the heat source, the magnitude of the magnetic field, and thermal conductivity of FCI; (2) the instability and periodicity of the fluid flow are primarily related to the unsteady reverse flow, which rises up and falls down periodically in the bulk region; (3) the physical mechanism of unsteady flow influenced by reverse flow, pressure drop, and Lorentz force has been concluded. It has been discovered that the breakdown of a reverse flow vortex causes a rapid reduction in pressure drop. (4) To avoid this phenomenon in engineering, a phase map of unsteady and steady flows in the DCLL blanket has been created. (5) The quasiperiodic characteristics of solid (flow channel insert) affected by flow are found and analyzed.

1. Introduction

The DCLL blanket is one of the most competitive candidate blankets for the tokamak device, which is a helium-cooled ferritic structure with a self-cooled PbLi breeder zone that uses /SiC flow channel insert (FCI) as an electric and thermal insulator [1]. Magnetohydrodynamic (MHD) mixed convection of upward flows under a strong transverse magnetic field and a large volumetric heat source in the DCLL blanket is considered (see Figure 1). The applied model in this study is one flow duct with FCI (poloidal orientation) from the DCLL blanket [2, 3]. Many studies have been conducted to analyze the model, and a majority of them do not consider buoyancy effects [4–6]. In the DCLL DEMO blanket, a large neutron heat source is generated, and the Grashof number (a dimensionless number, describing the ratio of buoyancy to viscous force) can reach up to 2.0×10^{12}. The results in [7] showed the key role of the buoyant effect on MHD flow in the blanket. As the heat source is an approximately exponential distribution [4], Vetcha et al. [8] proposed an approximate solution for MHD mixed convection under an exponential heat source. Several articles [9–12] have examined the impact of magnetic fields on fluid flow and heat transfer when considering heat sources and Joule heating. However, studies about buoyancy effects in the complex DCLL blanket are rare at present, while buoyancy plays a key role in the flow of a blanket. This work is motivated by the study of the mixed convection flow properties, heat transfer, and dynamical

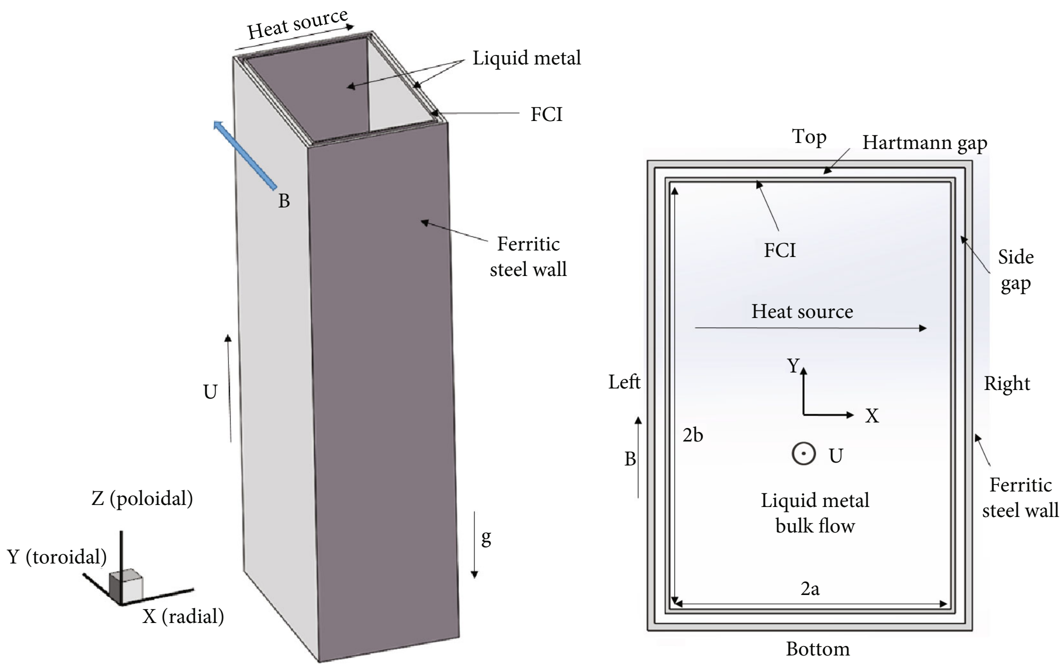

(a) 3D view (b) 2D view (outlet section)

Figure 1: Geometry of the rectangular channel flow with FCI. The geometry consists of four parts, namely, the bulk region, FCI, gap region, and ferritic steel wall. The fluid flows upward along the z-axis (poloidal direction) in the bulk region and gap region, the magnetic field is along the y-axis (toroidal direction), and the heat source decays along the x-axis (radial direction).

behaviors of FCI in the complex DCLL blanket and provides a numerical reference for the design and manufacture of blankets.

Under a magnetic field, unsteady flow affected by buoyancy has been recently discovered [13, 14], which showed the characteristics of low frequency, high amplitude, and periodicity. The unsteady flow with quasiperiodic fluctuation also has been observed in the experiments [15, 16]. Without an imposed magnetic field, the secondary instabilities of unsteady flow could break down into turbulence at large Gr [17], and flow instability was found in both numerical [18] and experimental studies [19, 20]. But under a magnetic field, the secondary instabilities would be shifted to larger jet amplitude, and the turbulence was suppressed [14]. Zhang and Zikanov [21] concluded that instability of the quasiperiodic unsteady flow of a vertical downward channel flow could be identified by a parameter $Gr/(Ha\,\mathrm{Re})$. Burr et al. [22] conducted an experimental study of heat transport in a turbulent MHD duct flow. The experiments exhibited typical random turbulent fluctuations when $Ha = 0$, but the fluctuations showed quasiperiodic patterns when $Ha = 4800$. Zikanov et al. [13–16, 21] investigated the vertical downward flow of MHD in pipe and duct with heat flux. The periodicity was also found in a cavity without a magnetic field [23]. The experimental results of Khanal and Lei [24] clearly show that reverse flow can occur at the outlet due to buoyancy effects. Akhmedagaev et al. [25] numerically analyzed the mixed convective flow in a horizontal duct with a heated bottom wall and a horizontal transverse magnetic field. The effects of the Reynolds number, Hartmann number, and Grashof number on the flow characteristics were investigated. Their study focused on the convective instability of the quasi-two-dimensional state under the influence of a strong magnetic field and determined the range of existence for this state. Linear stability analysis and numerical simulations of the nonlinear regime demonstrated that the large-scale low-frequency magnetic convection fluctuations were induced by the instability over a wide range, and their intensity did not diminish with increasing magnetic field strength.

Multiphysical effects caused by magnetic, thermal, and flow fields have an impact on the FCI. Li et al. [26] studied the structural safety of FCI considering thermal, hydrodynamic, and elastic issues in the DCLL blanket. Ali et al. [27] showed that the fluid-structure interaction would result in the structure oscillating at its fundamental frequency and might cause maximum limit stress or fatigue damage. The large amplitude fluctuations of temperature with large Gr and Re [13–16, 21] might cause some potential problems of FCI. Through experiments and numerical research conducted in a strong magnetic field, Brēķis et al. [28] investigated the practical application of silicon carbide FCI in lithium-lead liquid metal fluids. The experiments were conducted at temperatures reaching 700 Â°C and under a 5 T direct current magnetic field generated by a superconducting magnet. The researchers evaluated the impact of the insert on the hydrodynamic resistance of the liquid metal by measuring its pressure and integral flow rate. Additionally, they recorded the potential distribution on the channel wall to assess the velocity distribution of the liquid metal. The outcomes of their experiments provided crucial insights for the design of FCI.

In the majority of past studies, the influence of temperature buoyancy was not taken into consideration. However, in magnetic confinement thermonuclear fusion reactors, where the liquid cladding modules reach a height of about 2 meters, thermal buoyancy has a nonnegligible effect on the poleward flow. Hence, in this paper, we consider mixed convection because temperature buoyancy can lead to the instability of the entire flow, which is significantly different from forced convection. Additionally, we take into account the effects of the temperature field and flow field on structural deformation and its mechanical behavior. Since structural safety is of the utmost concern, it is not consistent with the reality that FCI is typically handled as a rigid body without taking its structural deformation into account. In this paper, we conducted an in-depth study on the importance of cold helium gas and FCI thermal conductivity on the convection structure and instability, a topic that has not been thoroughly analyzed in previously published research.

The aim of the present work is to study the unsteady buoyancy-aided up flow and mechanical behaviors of structure in the magneto-thermo-fluid-structure multiphysics coupled field of the DCLL blanket. Much literature reported that relevant studies focused on a single channel or adopted a 2D model. We hope to explore the flow in the complex chamber of the blanket, including flows in the bulk and gap regions, and the effects of unsteady flow. A 3D complex model with nondimensional numbers near blanket working conditions is adopted in this paper. The current work is a continuation of our previous work [7], in which the flow in the DCLL blanket was a steady-state flow suppressed by a strong magnetic field ($B \geq 3T$). We consider the following questions in this work:

(1) Does the breakdown of elevator mode and periodicity exist at high Re, high Gr, and moderate magnetic field ($B < 3T$) in a complex chamber typical for blankets?

(2) What are the properties of such an unsteady flow?

(3) Which parameters in the complex model have impacts on the unsteady flow, and what are their effects?

(4) What are the mechanical behaviors of FCI affected by unsteady flow?

The organizational structure of this chapter is as follows: Section 2 provides the definition of the problem. Section 3 presents the governing equations and parameters and describes the numerical algorithms, model settings, boundary conditions, and verification methods used. Section 4 covers the results and discussion, including the effects of helium cooling and seed heating, magnetic field influence, FCI thermal conductivity, and the dynamic behavior of FCI. The conclusion is summarized in Section 5. In order to enhance readability, Nomenclatures, Greek Symbols, and Acronyms are utilized in this study.

2. Physical Model

The physical model investigated is shown in Figure 1, which is a straight poloidal channel with an FCI inside it. The radial, toroidal, and poloidal directions in the DCLL model are defined as the x-axis, y-axis, and z-axis, respectively. The ferritic steel wall is cooled by the helium gas. The region inside the FCI is the so-called bulk region, and the region between the FCI and the ferritic wall is called as gap region. Heat source decreases exponentially along the X (radial) direction. Buoyancy-assisted upward MHD mixed convection in the bulk and gap region under a transverse strong magnetic field is considered. The material property of PbLi is referred to [29, 30], and FCI and the ferritic wall are referred to [26]. The parameter used in this paper is shown in Table 1. It should be noted that parameters in different designs are variable and still under optimization, and parameters in a typical model are adopted in this paper [4, 31].

The PbLi fluid in the DCLL blanket is heated by a volumetric heat source varying exponentially along the radial direction, as shown in Eq. (8) [4, 8]. Here, a is half the width of the bulk region, Q_0 is the maximum value of volumetric heat source value, and $Q_0 = 3 \times 10^7 \mathrm{J/(m^3 \cdot s)}$ is adopted. The heat source is only applied to the bulk region in this paper. Because the width of the gap region is very thin, the heat source from the reaction of neutron and lithium is omitted. Besides, the heat source in the ferritic wall and FCI is sufficiently small to be negligible.

Numerical simulation of MHD mixed convective flows poses a unique challenge due to the combination of retarding Lorentz forces and buoyancy. Due to the MHD effect, a large velocity gradient exists in both the Hartmann and side boundary layers, which are much thinner than the boundary layers of ordinary fluid flow, and a finer mesh and a smaller time-step are needed to simulate precisely the MHD flow. Due to the buoyancy effect, mixed convection requires more physical time to reach a fully developed state than forced convection. In this simulation of the DCLL blanket, mixed convection takes 7~15 times longer than forced convection. Besides, the complex geometry of the DCLL blanket results in a longer computation time than a single channel.

3. Basic Equations and Numerical Algorithm

The flows in the blanket are affected by the large heat source, strong magnetic field, and the thermal conductivity of FCI. The fluctuations of fluid velocity, temperature, and pressure would cause structural vibration, and the coupling effects of multiphysical fields have a great influence on each other. The basic equations and boundary conditions describing the multiphysics coupled field are displayed in this section.

In this paper, the following assumptions are adopted: (1) Buoyancy is calculated through the Boussinesq assumption; (2) Joule heating ($\vec{j}^2/\sigma$) is much smaller than the heat source, so then it can be neglected in the present simulation; and (3) the /SiC material is isotropic at small deformations.

3.1. Fluid Region. Considering the above assumptions, the continuity equation, Navier-Stokes equation, energy equation, and electric Poisson equation are shown below:

$$\nabla \cdot \vec{u} = 0, \tag{1}$$

Table 1: Typical blanket channel parameter.

Poloidal length	2 m
FCI channel inner sizes	$0.288\,m * 0.188\,m\ (Y * X)$
FCI thickness	0.005 m
FCI electrical conductivity	20 S/m
Gap width	0.008 m
Ferritic wall thickness	0.005 m
Inlet velocity of PbLi	0.06 m/s
Inlet temperature of PbLi	733 K
Helium temperature	673 K
Volumetric heat source	3×10^7 J/(m^3·s)
Heat transfer coefficient in helium	4000 W/(m^2·K)

$$\frac{\partial \vec{u}}{\partial t} + \left(\vec{u} \cdot \nabla\right)\vec{u} = -\frac{1}{\rho_0}\nabla P + \nabla\left(\nu\nabla\vec{u}\right) + \frac{1}{\rho_0}\left(\vec{j} \times \vec{B}\right) + g[1 - \beta(T - T_{\text{ref}})], \tag{2}$$

$$\rho_0 C_p\left(\frac{\partial T}{\partial t} + \nabla \cdot \left(\vec{u}T\right)\right) = \nabla \cdot (\kappa \nabla T) + q''', \tag{3}$$

$$\nabla \cdot (\sigma \nabla \varphi) = \nabla \cdot \left(\sigma \vec{u} \times \vec{B}\right). \tag{4}$$

Induced electric currents should satisfy Ohm's law (Eq. (5)). By using a consistent and conservative scheme [32, 33], the electric current conservation law is guaranteed even for a strong magnetic field. $T_{\text{ref}}(z)$ in Eq. (2) is the reference temperature, which is the mean temperature on a cross-section perpendicular to the flow direction and calculated in Eq. (7). According to the theoretical derivation [8], when a heat source is involved, the reference temperature T_{ref} should be handled as a function of z as the fluid absorbs thermal energy while flowing upward, which is the right way in order to study mixed convection.

$$\vec{j} = \sigma\left(-\nabla\varphi + \vec{u} \times \vec{B}\right), \tag{5}$$

$$\nabla \cdot \vec{j} = 0, \tag{6}$$

$$T_{\text{ref}}(z) = \frac{1}{4ab}\int_{-a}^{a}\int_{-b}^{b} T(x, y, z)dz. \tag{7}$$

The Reynolds number is $\mathrm{Re} = UL/\nu$, the Prandtl number is $\mathrm{Pr} = \nu\rho C_p/\kappa$, and the Hartmann number is $Ha = BL\sqrt{\sigma/\rho\nu} = Bb\sqrt{\sigma/\rho\nu}$. For the real working conditions of the DCLL blanket, Reynolds number can reach as high as 60000 and Hartmann number as high as 12000 [2]. Our simulation results show that mixed convection dominates the flow in the DCLL blanket. In order to get a better explanation of the buoyancy effects on the MHD flow and the physical mechanism of mixed convection in the blanket, we introduce three definitions of the Grashof number. The original definition of the Grashof number is shown in Eq. (9). The ΔT in the Grashof number can be measured in two ways, one is by the heat source Q and the other is by the temperature difference. The Grashof number measured by the heat source Q is defined as Gr_Q, and the expression is given by Eq. (10). The ΔT in Gr_Q is defined as $\Delta T = \bar{Q}L^2/\kappa$, where $\bar{Q}$ is the average value of heat source $Q(\bar{Q} = (1/4ab)\int_{-a}^{a} Q(x, y)dxdy)$. The definition method of Gr_Q is widely adopted in the blanket [2, 8, 34]. The Grashof number, which is measured by the temperature difference between helium and the fluid, is defined as Gr_{He} (as shown in Eq. (11)). In Gr_{He}, the temperature difference ΔT is the difference between the fluid inlet temperature T_{inlet} and the helium temperature T_{He}. The Grashof number, which is measured by the internal temperature difference of the fluid, is defined as the local Grashof number Gr_{loc} (as shown in Eq. (12)). In the Gr_{loc}, the temperature difference ΔT is the difference between the highest temperature $T_{\max}$ and the lowest temperature $T_{\min}$ on a cross-section perpendicular to the flow direction. Due to the continuous heating of the heat source, the temperature difference is usually greatest at the outlet, and the cross-section is set at the outlet.

$$Q(x) = Q_0 \cdot \exp\left(-\frac{x + a}{a}\right), \tag{8}$$

$$Gr = \frac{g\beta\Delta T L^3}{\nu^2}, \tag{9}$$

$$Gr_Q = \frac{g\beta\Delta T L^3}{\nu^2} = \frac{g\beta L^5\bar{Q}}{\nu^2 \cdot \kappa}, \tag{10}$$

$$Gr_{\text{He}} = \frac{g\beta\Delta T L^3}{\nu^2} = \frac{g\beta(T_{\text{He}} - T_{\text{inlet}})L^3}{\nu^2}, \tag{11}$$

$$Gr_{\text{loc}} = \frac{g\beta\Delta T L^3}{\nu^2} = \frac{g\beta(T_{\max} - T_{\min})L^3}{\nu^2}. \tag{12}$$

Nondimensional temperature θ is defined as

$$\theta = \frac{T - T_0}{T_0 - T_{\text{He}}} = \frac{T - T_0}{\Delta T}, \tag{13}$$

where T_0 is the inlet temperature of the fluid and T_{He} is the temperature of helium gas. The wall Nusselt number for FCI is defined in Eq. (14) [7], which represents the ratio of thermal convection and conduction between the bulk region and the FCI.

$$Nu_{\text{wall}} = \frac{\int (\partial\theta/\partial n)dA}{\int dA}. \tag{14}$$

3.2. Solid Region. The dynamic fluid-structure interaction is investigated based on the consideration of the influence of fluid fields on the FCI mechanical behaviors. In this study, it is supposed that the FCI has small deformations and the influence of solid deformation on the fluid field is neglected. The aim of FCI's dynamical behavior analysis is to investigate the influence of buoyancy on the deformations and stresses of the FCI structure. The relation of strain and displacement, the constitutive equation, and the equilibrium equation are shown below:

$$\varepsilon_{ij} = \frac{1}{2}\left(d_{i,j} + d_{j,i}\right) + \alpha \Delta T \delta_{ij},$$
$$\sigma_{ij} = 2G\varepsilon_{ij} + \lambda \Theta \delta_{ij}, \quad (15)$$
$$\sigma_{ij,j} + F_i = \rho \frac{\partial^2 d_i}{\partial t^2}.$$

In these equations above, ε_{ij}, d_i, α, ΔT, and δ_{ij} denote strain tensor, ith component of the displacement vector, thermal expansion coefficient, temperature difference between the inner and outer wall of FCI, and Kronecker delta, respectively. σ_{ij}, G, λ, and Θ represent stress tensor, shear modulus, Lame constant, and volumetric strain, respectively. The Lame constant is defined as $\lambda = E\mu'/[(1+\mu')(1-2\mu')]$, where μ' is Poisson's ratio. F_i is the ith component of volumetric force.

For structural dynamics, the finite element method is a commonly used numerical solution approach. In this study, the finite element method is employed to solve the thermal deformation of FCI in multiphysics coupled fields. The static fluid-structure interaction is investigated using the sequential coupling method. Initially, the FVM is utilized to solve the fluid field and the conjugate heat transfer. Subsequently, the interface temperature between the fluid region and the FCI structure is extracted as the boundary data for structural analysis. Finally, the FEM is employed to analyze the deformation field and stress field in FCI. The overall procedure is summarized in Figure 2. Due to the regular shape of the FCI model, the 8-node hexahedral elements are applied to analyze the displacements. Considering the small deformation and linear elasticity of FCI, the strain resulting from the thermal fluid is computed by geometric equations and the stress is evaluated by Hooke's law.

3.3. The Boundary Conditions. For the inlet boundary condition, velocity ($U = 0.06$ m/s) and temperature ($T_0 = 733$ K) are fixed. Neumann's boundary condition is adopted for electric potential ($\partial\varphi/\partial n = 0$) and pressure ($\partial p/\partial n = 0$).

For the outlet boundary conditions, pressure is fixed to be zero, and electric potential and temperature satisfy the Neumann boundary condition ($\partial T/\partial n = 0$ and $\partial\varphi/\partial n = 0$). Convective boundary condition [35] ($(\partial u/\partial t) + u_0(\partial u/\partial n) = 0$), which is an opening boundary condition that prevents outlet flows from generating significant distortion, is employed for outlet velocity:

Conjugate heat transfer and electrical conductivity occur at the interface between fluid and solid regions. At the interface, boundary conditions for temperature, electric potential, current, and velocity satisfy $T_{\text{fluid}} = T_{\text{solid}}$, $\varphi_{\text{fluid}} = \varphi_{\text{solid}}$, $\vec{j}_{\text{fluid}} \cdot \vec{n}_{\text{fluid}} = \vec{j}_{\text{solid}} \cdot \vec{n}_{\text{solid}}$, and $\vec{u} = 0$.

The outside wall of the blanket is cooled by the coolant helium gas, electric potential meets the needs of electric insulation ($\partial\varphi/\partial n = 0$), and the third boundary condition ($\kappa(\partial T/\partial n) + h(T - T_{\text{He}}) = 0$) is applied for temperature.

For the structural analysis of FCI, the boundary condition of displacement is applied according to the installation of FCI in a blanket. At the inlet end, $d_z = 0$. At the outlet end, $d_x = d_y = 0$.

3.4. Numerical Algorithm. The solver used in this paper has been developed and verified in our previous work [7]. This method is currently the most widely used approach in numerical calculations of flow field and heat transfer [36–39]. Based on the finite volume method (FVM), a validated magnetic-convection solver with a consistent and conservative scheme of electrical current is developed. The PISO algorithm on unstructured collocated meshes is employed to solve the flow fields, conjugate temperature fields, and electrical current fields. Meanwhile, the finite element method (FEM) is used to investigate the mechanical behaviors of the FCI structural field. The algorithm process is as follows:

(1) Initialization: load the mesh and initial physical fields

(2) Solve the Navier-Stokes equations to obtain the velocity u at the grid center

(3) Solve the pressure Poisson equation

(4) Correct the velocity and velocity flux

(5) Solve the Poisson equation for electric potential to obtain the current flux on the grid surface

(6) Interpolate the current flux from the surface to the grid center

(7) Calculate the Lorentz force based on the current at the grid center

(8) Solve the energy equation to obtain the temperature field

(9) Update the velocity field, electric field, and temperature field

(10) Begin the calculation for the next time step, repeating the process from (2) to (9)

The grid independence verification adopts the model in Figure 1, which contains upward flows in the bulk and the gap region, with $B = 0.7$ T, $\kappa_{\text{FCI}} = 2$ W/(m·K), $\text{Re} = 31000$, and $Gr = 3.5 \times 10^{11}$. The Hartmann number can characterize the thickness of the Hartmann layer and the side layer. The Hartmann layer is located on the wall surface perpendicular to the magnetic field, with a thickness equal to b/H a, while the side layer is located on the wall surface parallel to the magnetic field, with a thickness equal to $b/\sqrt{Ha}$. To describe the flow and heat transfer more precisely in the Hartmann layer and side layer, at least 4 layers and 6 layers of grids are discretized, respectively, and transition gradually from the first layer grid with a ratio of 1.2. Three sets of grids are used to study the grid sensitivity, namely, coarse grid, medium grid, and fine grid. The convergence of grids is displayed in Table 2. It shows that the relative error of the mean Nusselt number between the medium grid and the fine grid is 0.96%, indicating the grid independence of the numerical results. The mean Nusselt number is time-averaged over

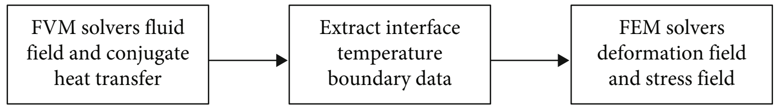

Figure 2: The working process of static fluid-structure interaction.

Table 2: The computational results of wall Nusselt numbers under different discrete grids.

Mesh	Grid	Nu_{mean}	Relative error
Coarse	$105 \times 136 \times 80$	50.32	2.98%
Medium	$135 \times 177 \times 100$	49.33	0.96%
Fine	$178 \times 229 \times 120$	48.86	–

Table 3: Summary of the flow parameters of the three examples and the corresponding Grashof number ($\mathrm{Re} = 31000$, $B = 1\,\mathrm{T}$, and $Ha = 3200$).

Case	Q (J/(m^3·s))	T_{He} (K)	Gr_Q	Gr_{He}	Gr_{loc}
A	3×10^7	673	3.5×10^{11}	2.45×10^9	2.08×10^9
B	3×10^7	733	3.5×10^{11}	0	1.75×10^9
C	0	673	0	2.45×10^9	6.3×10^8

serval periods. Medium mesh is adopted in the following DCLL blanket simulations.

4. Results and Analysis

In this section, factors that cause flow instability in the blanket and their roles are discussed. According to the results, the temperature difference between helium gas and PbLi fluid ($\Delta T_{He,f}$), the large neutron heat source, the weak magnetic field, and the big FCI's thermal conductivity could cause an unsteady flow. In the following analysis, the hot wall (left side wall) represents the side wall near a large heat source, the cold wall (right side wall) is used to represent the side wall near a small heat source, the centerline perpendicular to the magnetic field at the outlet is simply called the outlet centerline. The effects of the temperature of He gas, heat source, magnetic field, FCI's thermal conductivity on unsteady flow, and mechanical behaviors of the structure are investigated. Effects of unsteady flows and thermal conductivity of FCI would result in some interesting phenomena, which have not been reported in previous literature, and the mechanisms of these phenomena are investigated.

4.1. Effects of Helium Cooling and Neutron Heat Source. Under a weak magnetic field, two factors, the temperature difference of helium gas and inlet fluid $\Delta T_{He,f}$ and heat source Q, would cause the unsteady flow. The roles of flow instability in the DCLL blanket are investigated through the design of three numerical cases. The setting conditions for the three cases are concluded in Table 3. The conditions of cases A, B, and C remain unchanged, except for the heat source and helium gas temperature. Reynolds number, magnetic field, and the thermal and electrical conductivity of FCI κ_{FCI} are fixed at 31000, 1 T, $\kappa_{FCI} = 2\,\mathrm{W/(m \cdot K)}$, and 20 S/m in these three cases, respectively. In case A, the maximum heat source Q_0 and helium gas temperature T_{He} is set to $3 \times 10^7\,\mathrm{J/(m^3 \cdot s)}$ and 673 K, respectively. In case B, the maximum heat source Q_0 is set to $3 \times 10^7\,\mathrm{J/(m^3 \cdot s)}$ and helium gas temperature is set to the same as the inlet temperature of PbLi fluid (733 K). In case C, the heat source is set at 0, and the helium gas temperature is set to 673 K.

In case A, $Gr_Q = 3.5 \times 10^{11}$ and $Gr_{He} = 2.45 \times 10^9$. After the unsteady flow reaches fully developed status, a mean value of local Grashof number Gr_{loc} at outlet equals to 2.08×10^9. An unsteady flow occurs due to the thermal-shear instability which cannot be suppressed by a weak magnetic field. The flow exhibits characteristics of unsteady quasiperiodicity motion. As shown in Figure 3(a), due to the cooling effect of helium gas, a reverse flow appears near the cold wall. The reverse flow moves upward and down in the motion zone and it also exhibits quasiperiodic characteristics.

In case B, $Gr_Q = 3.5 \times 10^{11}$ and $Gr_{He} = 0$, and the mean value of the local Grashof number Gr_{loc} at outlet equals to 1.75×10^9. In Figure 3(b), a slight unsteady flow also occurs, and the unsteady reverse flow has a small amplitude oscillation. The flow pattern and instability in case B are similar to that in case A. The comparison of outlet velocities between cases A and B is shown in Figure 4, and the amplitude of velocity of case B is smaller than that of case A. Besides, the motion zone of case B is smaller than that of case A, indicating that the instability of case B is weaker than case A.

In case C, $Gr_Q = 0$, $Gr_{He} = 2.45 \times 10^9$, and $Gr_{loc} = 6.3 \times 10^8$. In Figure 5, due to the lack of a heat source, the effects of the magnetic field and the remaining boundary conditions are symmetrical, which leads to the symmetry of the fluid field along the x-axis. In the initial state, symmetrical reverse flow occurs at two side layers. Then, the reverse flow quickly rushes to the bottom ($t = 15\,\mathrm{s}$). A drastic impingement

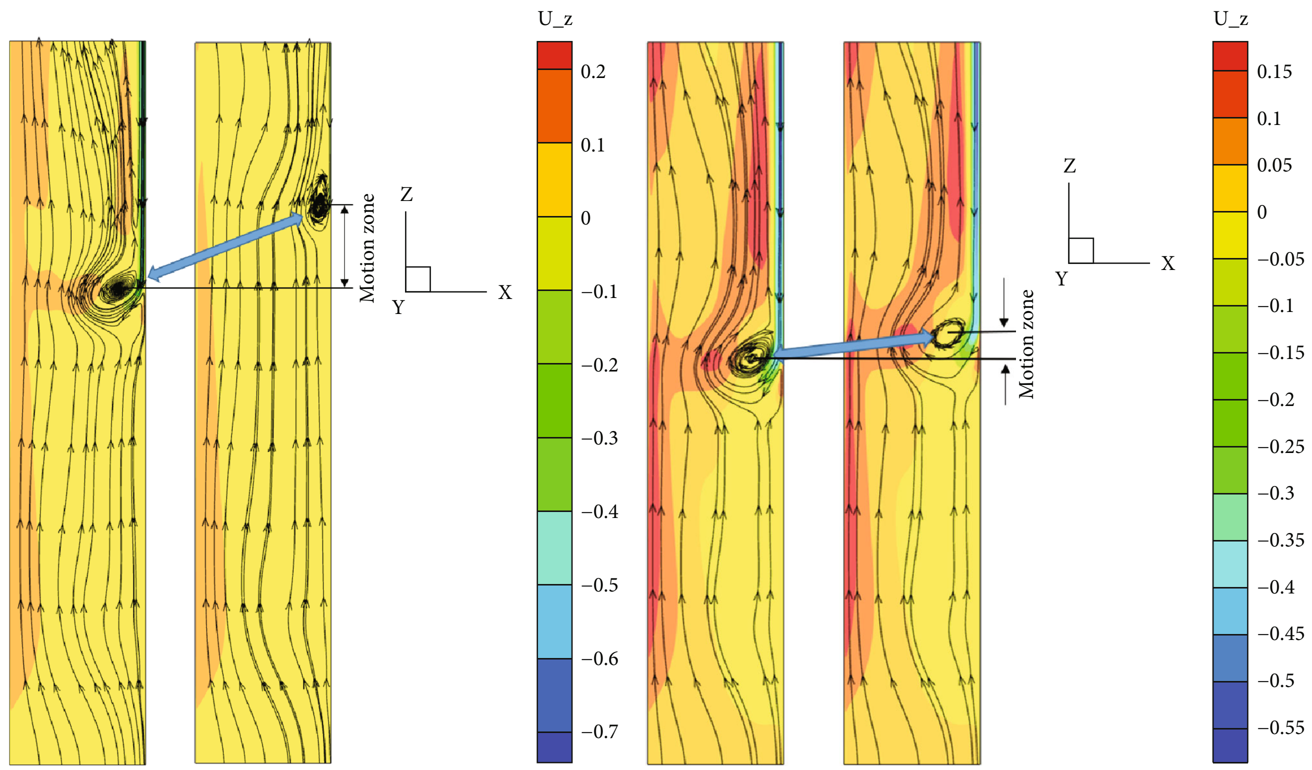

FIGURE 3: Streamline, the lowest and highest motion position, and motion zone of unsteady reverse flow in the bulk region. (a) $Gr_Q = 3.5 \times 10^{11}$ and $Gr_{He} = 2.45 \times 10^9$. (b) $Gr_Q = 3.5 \times 10^{11}$ and $Gr_{He} = 0$. Due to the higher helium gas temperature in case B compared to case A, the range of the motion region in case B decreases, and the instability is weakened.

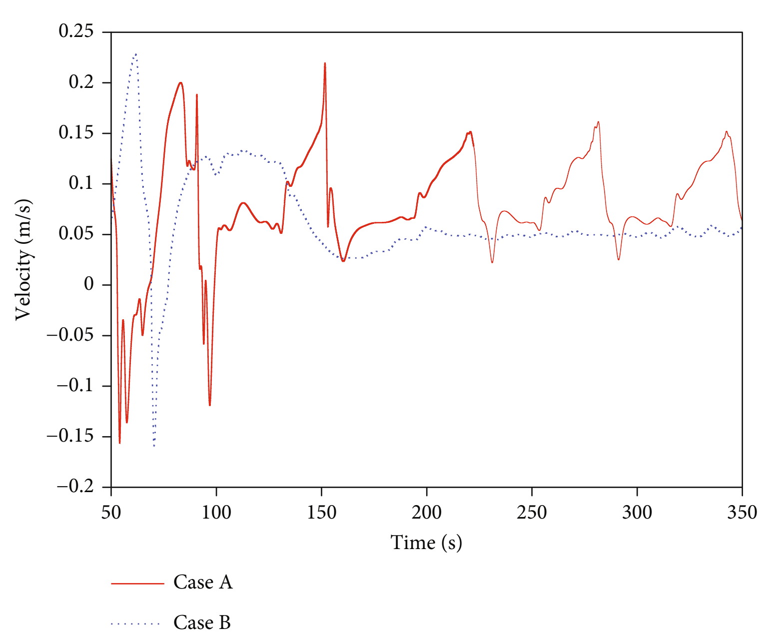

FIGURE 4: Outlet mid-point velocities of cases A and B change over time. After the flow has fully developed ($t > 200$ s), case B exhibits weak instability, while case A demonstrates quasiperiodic instability.

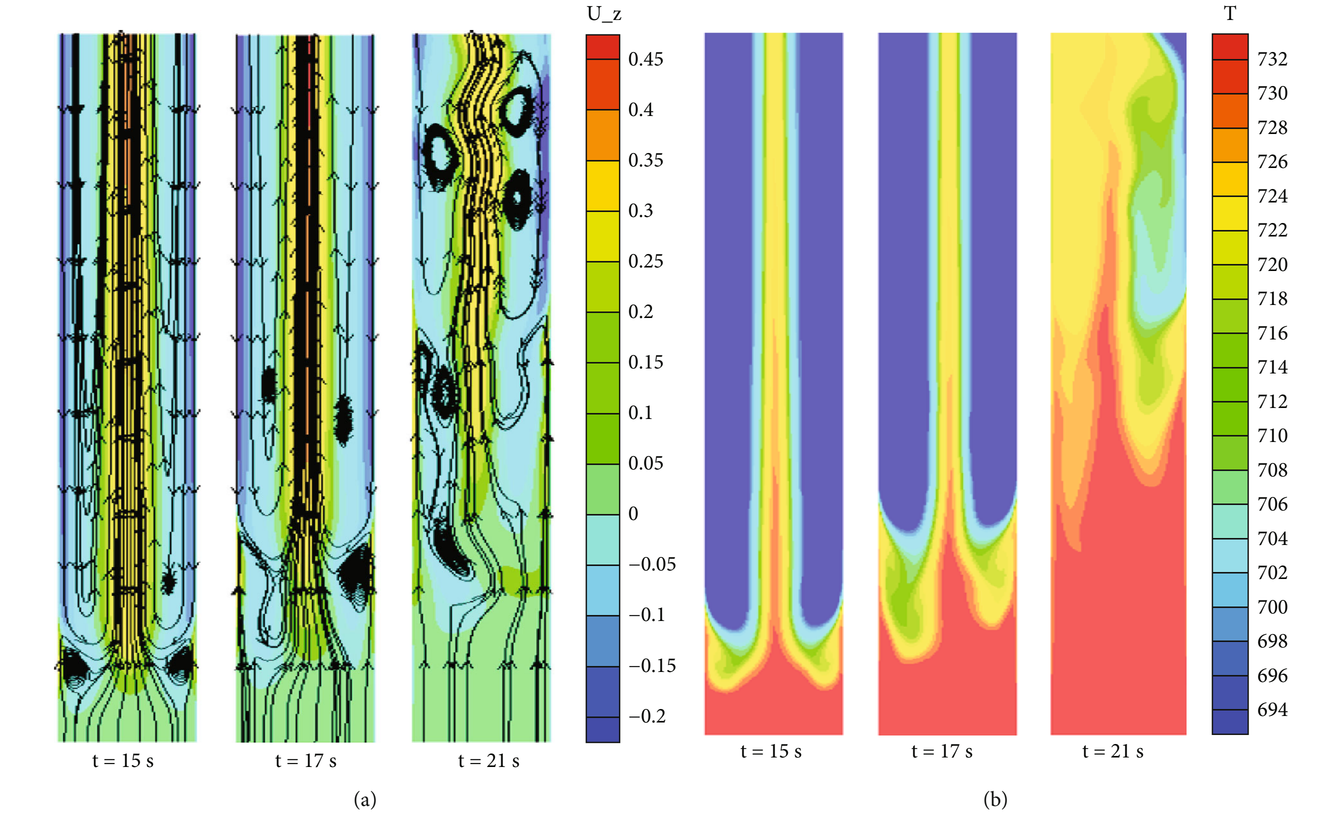

Figure 5: (a) Streamline and (b) temperature field in the bulk region change over time of center-plane ($Y = 0$) for the heat source $Q = 0$, case C. At $t = 15$ s, the flow is symmetric. At $t = 17$ s, disturbances caused by buoyancy disrupt the symmetry. At $t = 21$ s, the instability further increases.

between reverse flow and up flow occurs, and the flow shows the Kelvin-Helmholtz instability. The instability first occurs at the interface between reverse flow and up flow ($t = 17$ s), then spreads throughout the entire bulk region ($t = 21$ s). The temperature field and the velocity field are coupled to each other together. The unsteady velocity field induces the instability of the temperature field which aggravates the instability of the velocity field and eventually leads to the instability of the MHD flow field. It is the big temperature difference between helium gas and inlet fluid $\Delta T_{\mathrm{He},f}$ that leads to the instability of the flow field. Besides, the differences in flow structures among cases A, B, and C indicate that both the heat source and heat transfer between He gas and liquid metal dominate the flow pattern in the bulk region and have a strong impact on the instability of the flow field.

These different kinds of Grashof numbers are indicated in Table 3. As Gr_Q is measured by neutron heat source, Gr_Q in cases of $Q = 3 \times 10^7\ \mathrm{J/(m^3 \cdot s)}$ can reach 3.5×10^{11}. The mixed convection leads to stronger coupling effects and a more uniform distribution of the temperature field. Results imply that the coupling effects result in the local Grashof number dropping down to about 10^9. The local Grashof number in the DCLL blanket is not as big as generally recognized (of 1×10^{12} in the DCLL DEMO blanket [2], which is measured by heat source Gr_Q). Comparing these three cases, it can be indicated again that the instability of flow in the bulk region is influenced by the coupling effects of the neutron heat source and the temperature difference between helium gas and liquid metal. Although the Gr_{He} is small, it plays an important role in Gr_{loc} and instability. It can be concluded that under current blanket working conditions, temperature differences between helium gas and liquid metal play important roles in flow instability. To make the conclusions more precise, a conjugated heat transfer with the He gas can be considered in further research.

In this work, we found that the Gr_{loc} can provide an alternative perspective of the buoyancy effect. Gr_{loc} is a combination of helium temperature, FCI thermal conductivity, and so on. As we can see, cases A and B have different flow stability despite having the same Gr_Q. That means that the buoyancy effect on the flow in the blanket cannot be evaluated by only the strength of the heat source. Although the Grashof numbers measured by either heat source or temperature difference are the same, the buoyant impact on flow instability is different.

4.2. Effects of Magnetic Field. Because Lorentz force is a quadratic function of the magnitude of the external magnetic field, the magnetic field has a nonlinear influence on the fluid field and temperature field. An investigation of the magnetic field effects on fluid, thermal, and structure fields is conducted. Seven cases at the magnetic field to be $B = 0.7$ T, 1 T (case A), 1.5 T, 1.7 T, 2 T, 4 T, and 6 T are designed to analyze the MHD flow and heat transfer. The

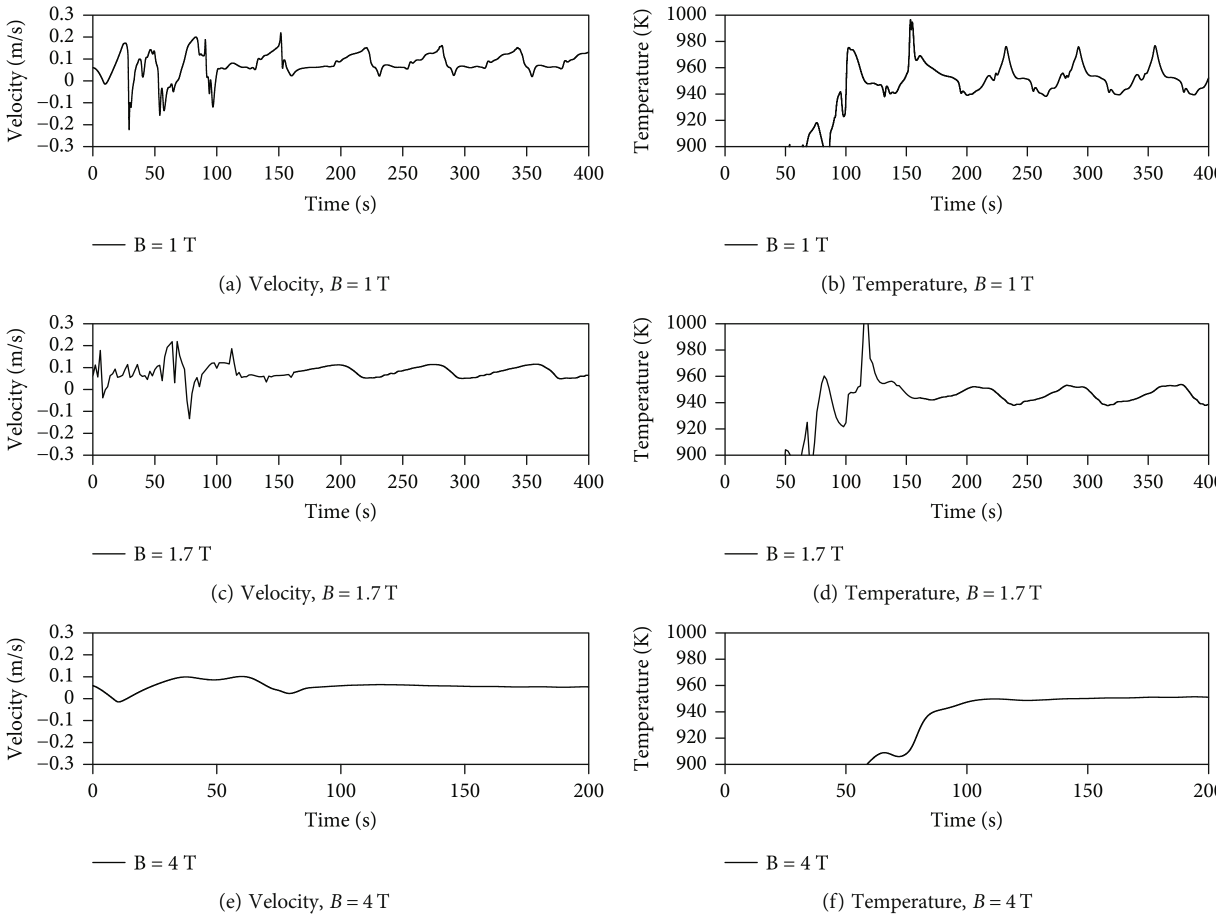

(a) Velocity, $B = 1$ T (b) Temperature, $B = 1$ T
(c) Velocity, $B = 1.7$ T (d) Temperature, $B = 1.7$ T
(e) Velocity, $B = 4$ T (f) Temperature, $B = 4$ T

Figure 6: Signals of velocity and temperature at outlet center-point ($x = 0$ m, $y = 0$ m, and $z = 2$ m) in the bulk region under different magnetic fields, $\kappa_{\text{FCI}} = 2$ W/(m·K). As the magnetic field increases, the instability weakens until it eventually disappears.

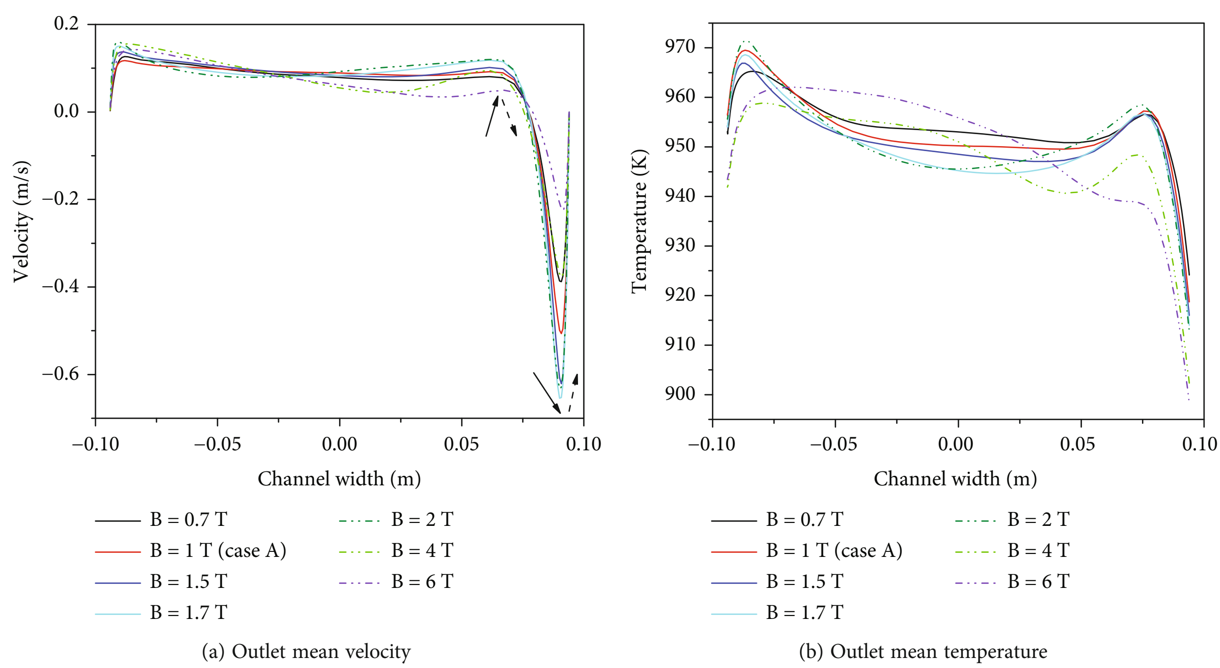

(a) Outlet mean velocity (b) Outlet mean temperature

Figure 7: Comparison of (a) mean velocity and (b) temperature profiles of outlet centerline between unsteady (solid line, $B \leq 1.7$ T) and steady (dash line, $B \geq 2$ T) cases. Case with $B = 1$ T is case A in Section 4.1.

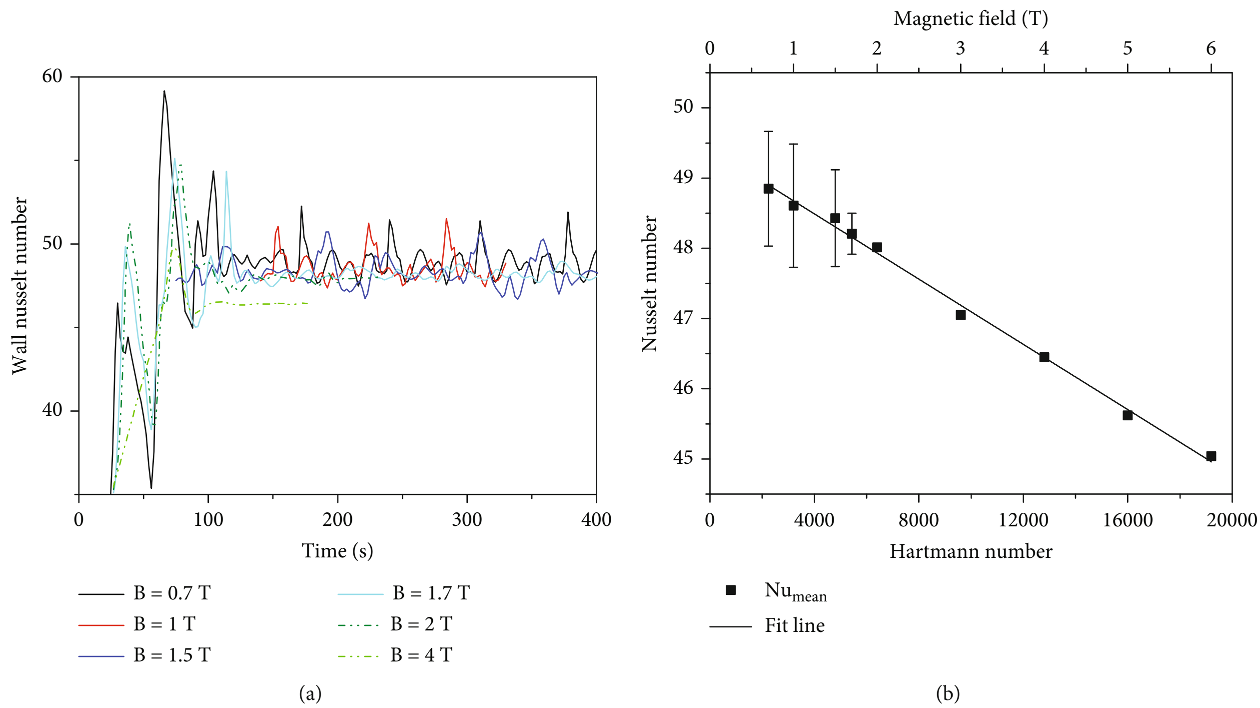

Figure 8: (a) Signals of the wall Nusselt number in the bulk region. (b) Mean wall Nusselt number, which has a linear relationship between the Hartmann number. $\kappa_{FCI} = 2$ W/(m·K) and $Gr_Q = 3.5 \times 10^{11}$.

FCI's thermal and electrical conductivity in all of the cases in this section is 2 W/(m·K) and 20 S/m, respectively. An unsteady flow would occur when the magnetic field is too weak to suppress the thermal-shear instability. The signals of velocity and temperature of $B = 1$ T, 1.7 T, and 4 T are shown in Figure 6. The flow fields at $B = 1$ T and 1.7 T are unsteady. But when the magnetic field reaches 4 T, the instability is suppressed. In Figure 6, we conducted an FFT (fast Fourier transform) analysis on the velocity and temperature time series after 100 seconds under different B. The corresponding peak frequencies for $B = 1$ T, $B = 1.7$ T, and $B = 4$ T are 0.01678, 0.01342, and 0, respectively. As the magnetic field increases, the instability of the flow gradually decreases, and the peak frequency gradually decreases. When the magnetic field reaches $B = 4$ T, the flow becomes stable with a peak frequency of 0. Under a weak magnetic field, the unsteady velocity and temperature field both show large amplitude, low frequency, and quasiperiodic characteristics after fully developed. The frequency and amplitude both depend on the magnetic field density.

For the suppression effect of the magnetic field, the flow field in the bulk region is a quasi-2D distribution parallel to the magnetic field direction. The velocity profile along the centerline at the outlet perpendicular to the magnetic field can almost represent the whole velocity field at the outlet. After the flows reach fully developed status, the mean velocity and temperature are obtained over several periods, the definition of the mean velocity field is $U_{mean} = \sum_{i=1}^{m} U/m$, and m is the all-time steps used to average the flow field. As shown in Figure 7(a), reverse flows occur in all cases due to the temperature difference of fluid on the cross-section of the duct. In these cases, the flow is unsteady when the magnitude of the magnetic field $B \leq 1.7$ T, but the flow is steady when $B \geq 2$ T. Figure 7 illustrates that the magnetic field has nonmonotonic effects on velocity and temperature. With an increase in the magnitude of the magnetic field, the mean velocity of reverse flow firstly increases in the unsteady region, then decreases in the steady region. As a result, the reverse flow reaches a maximum value when $B = 1.7$ T. The velocity variation of the reverse flow causes corresponding variations of the velocity and temperature at other locations in the flow field. As shown in Figure 7(b), the magnetic field has a greater impact on the temperature distributions of the bulk region at the center and near the cold wall and has a smaller influence on the temperature near the hot wall.

The variations of wall Nusselt number under different magnetic fields over time ($t = 0 \sim 400$ s) are shown in Figure 8(a). The wall Nu numbers of unsteady flow also exhibit quasiperiodic characteristics after fully developed. The fluctuation of the Nu number is suppressed by the enhanced magnetic field until it becomes steady. Averages of Nu number over several periods are shown in Figure 8(b). The error bar represents the standard deviation of the Nu number, which is calculated as $\sqrt{1/m\sum_{i=1}^{m}(Nu - 1/m\sum_{i=1}^{m}Nu)^2}$. Mean Nu numbers of unsteady flow and steady flow show an approximately linear relationship with the Ha numbers. A fit line of Nu with Ha between unsteady flow and steady flow is given below:

$$Nu_{mean} = -2.32 \times 10^{-4} \cdot Ha + 49.42. \tag{16}$$

Pressure drop is an important issue in the MHD study. Due

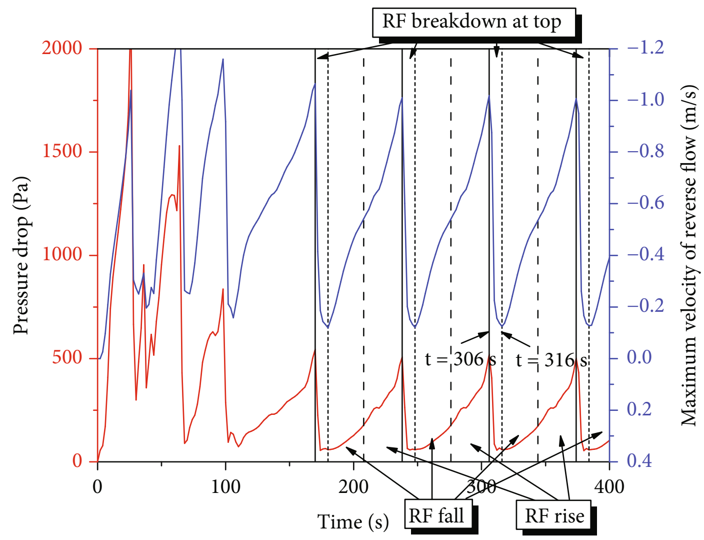

(a) Pressure and velocity of reverse flow (RF)

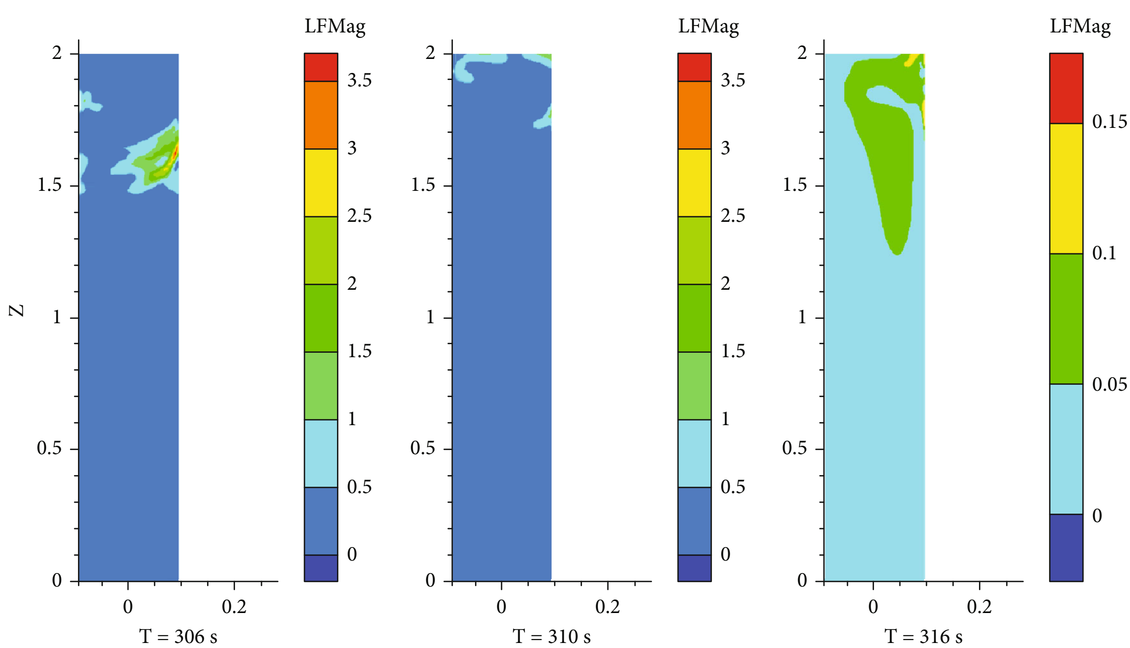

(b) Contour plots of Lorentz force

Figure 9: (a) Pressure drop (red line) and the velocity of reverse flow (blue line) and (b) Lorentz force change over time, $\kappa_{\mathrm{FCI}} = 2\,\mathrm{W/(m{\cdot}K)}$, $B = 0.7\,\mathrm{T}$, $Ha = 2240$, and $Gr_Q = 3.5 \times 10^{11}$. The pressure drop, velocity of reverse flow, and Lorentz force undergo synchronous temporal variations. The breakdown of reverse flow ($t = 306\,\mathrm{s} \sim 316\,\mathrm{s}$) results in a sudden decrease of pressure drop and Lorentz force.

to the flow dampening caused by the Lorentz force under a strong magnetic field, pressure drop has become an important factor to be considered in blanket design. For a steady flow of liquid metal fluid, lots of effort has been made to reduce pressure drop [31, 40, 41]. For unsteady flow, a new problem about pressure drop, fluctuation of pressure drop, comes out. The changes in pressure drop and the maximum velocity of reverse flow are shown in Figure 9(a). The quasiperiodic cycle of reverse flow can be divided into three phases, which are rise (move close to outlet), breakdown (breakdown at the top of the motion zone of reverse flow), and fall (move close to inlet). At the stages of fall and rise, both pressure drop and the maximum velocity of reverse flow increase. When reverse flow breaks down at the top, such as $t = 306 \sim 316\,\mathrm{s}$, the maximum velocity, pressure drop, and Lorentz force (as shown in Figure 9(b)) rapidly reduce during a short time. These changes indicate that pressure drop, velocity of reverse flow, and Lorentz force have an excellent corresponding relationship. The relationship reveals the physical mechanism that pressure drop has changed drastically. Firstly, in reverse flow falling and rising regions, reverse flow rises with a gradually increasing velocity. An increasing Lorentz force is generated according to Ohm's law. As the Lorentz force hinders the reverse flow from rising up, a larger inlet pressure is demanded to drive

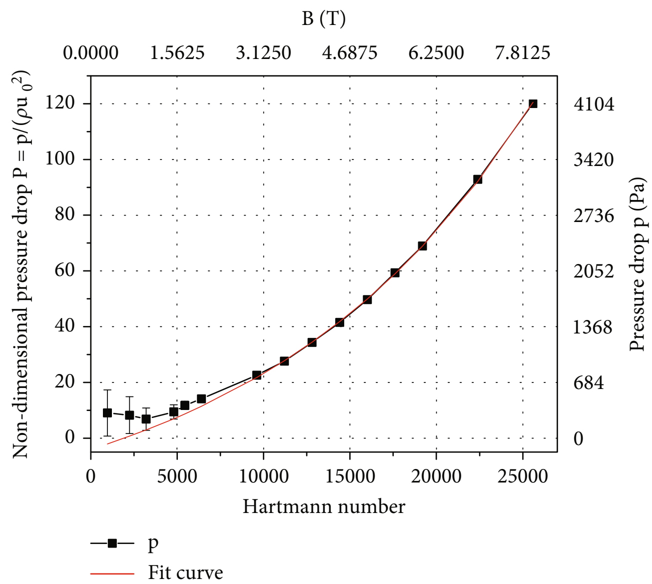

Figure 10: Nondimensional pressure drop under different Hartmann numbers, $\kappa_{FCI} = 2\ \mathrm{W/(m{\cdot}K)}$ and $Gr_Q = 3.5 \times 10^{11}$. Error bars indicate the amplitude of fluctuation of pressure drop. The formulation of the fit curve is $P = 31e^{6.3\times10^{-5}Ha} - 35$.

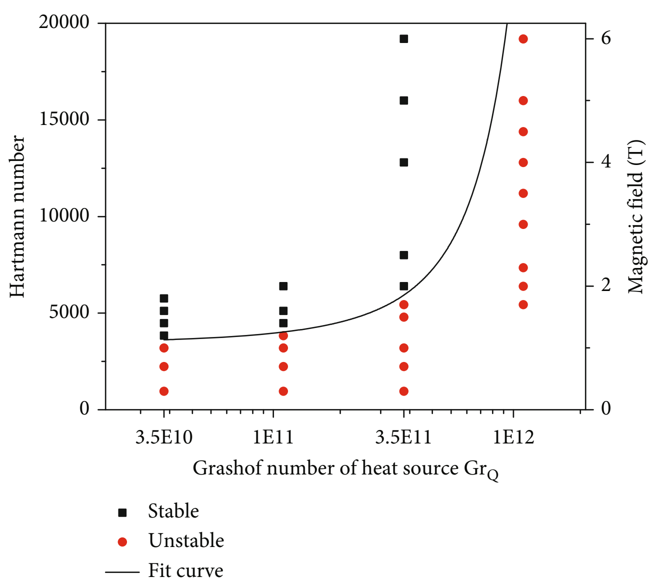

Figure 11: A phase map of unsteady and steady flow in the DCLL blanket. Two y-axis labels are used, the magnetic field is shown on the right y-axis, and the corresponding Hartmann number is on the left y-axis. At high Grashof numbers, it becomes more challenging to suppress instability using magnetic fields.

the reverse flow upward at a constant flow rate. Then, when the reverse flow reaches the top and the breakdown occurs, the reverse flow is weakened. Correspondingly, the Lorentz force drops down to the minimum, as it does the pressure loss due to the weakened Lorentz force. It should be noted that buoyancy increases the pressure drop by 1.04~1.23 times in a blanket [7]. Buoyancy is smaller compared to Lorentz force in reverse flow, and its effect on pressure drop is almost negligible.

Inlet pressure drops under different magnetic fields are shown in Figure 10, the nondimensional pressure drop $(P = p/\rho u_0^2)$ of steady flow has a linear relation with $e^{6.3\times10^{-5}Ha}$, and the formulation is

$$P = 31e^{6.3\times10^{-5}Ha} - 35. \tag{17}$$

Enhanced magnetic fields suppress the fluctuation of pressure drop and increase the mean pressure. For the pressure drop, the ratio of amplitude to mean value can reach 80.4% $(B = 0.7\ \mathrm{T},\ Ha = 2240)$, 58.6% $(B = 1\ \mathrm{T},\ Ha = 3200)$, 27.1%

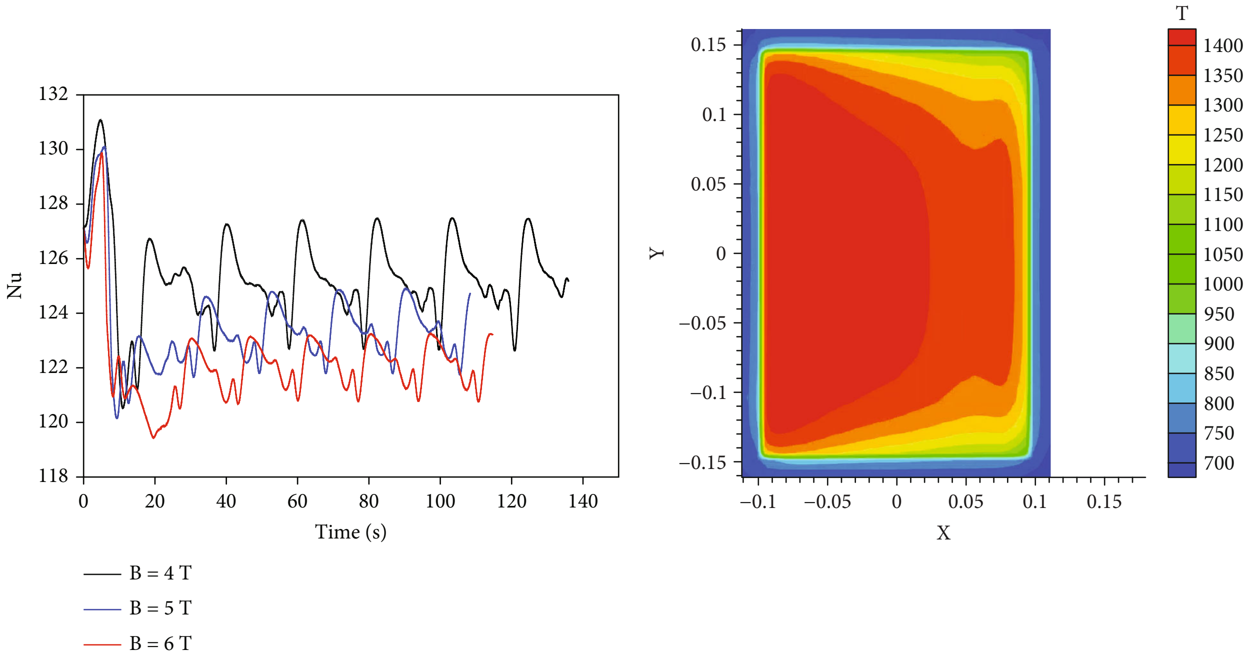

(a) (b)

Figure 12: (a) Nusselt number under different magnetic fields. (b) Temperature field, $B = 6\,\mathrm{T}$ ($Ha = 19200$). At high magnetic fields, the Nusselt number still exhibits instability due to the large Grashof number. As the magnetic field increases, the amplitude of the Nusselt number oscillations decreases, but it is not completely suppressed, $Gr_Q = 1.1 \times 10^{12}$.

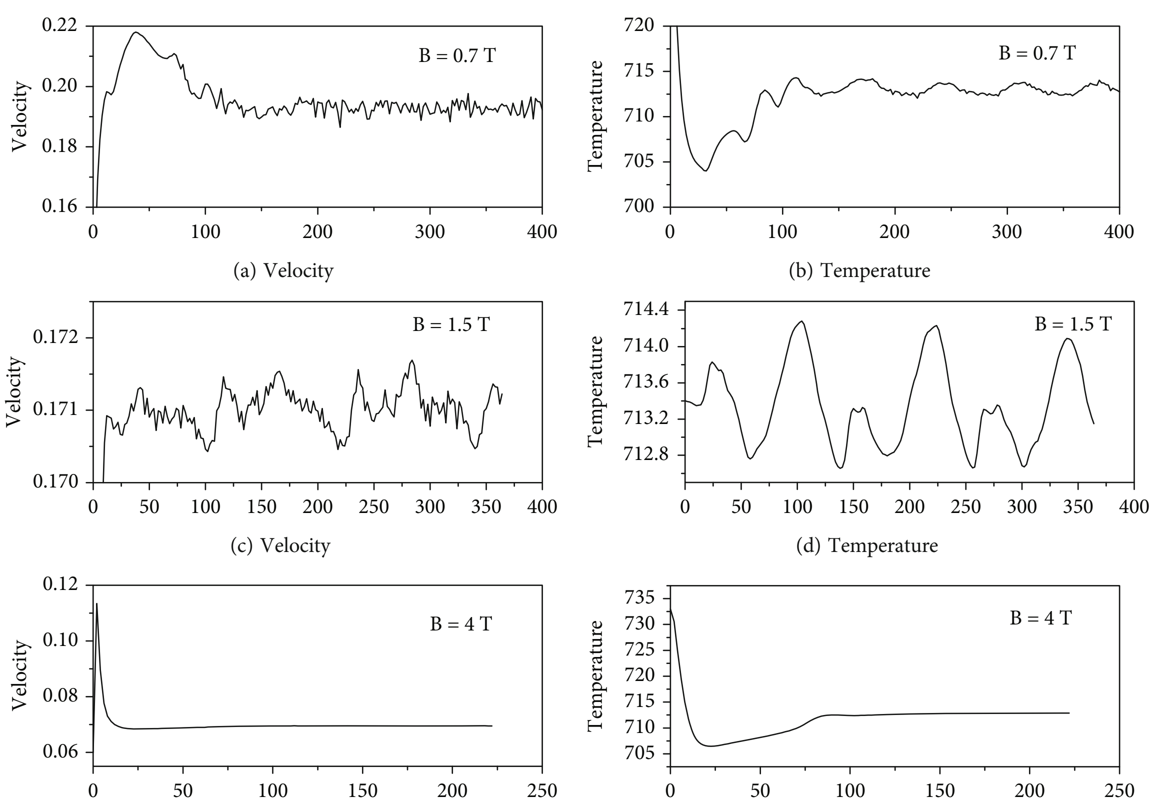

(a) Velocity (b) Temperature

(c) Velocity (d) Temperature

(e) Velocity (f) Temperature

Figure 13: Signals of velocity and temperature of outlet center-point in the side gap region under different magnetic fields, $\kappa_{\mathrm{FCI}} = 2\,\mathrm{W/(m \cdot K)}$ and $Gr = 3.5 \times 10^{11}$. At $B = 4\,\mathrm{T}$, the instability is completely suppressed.

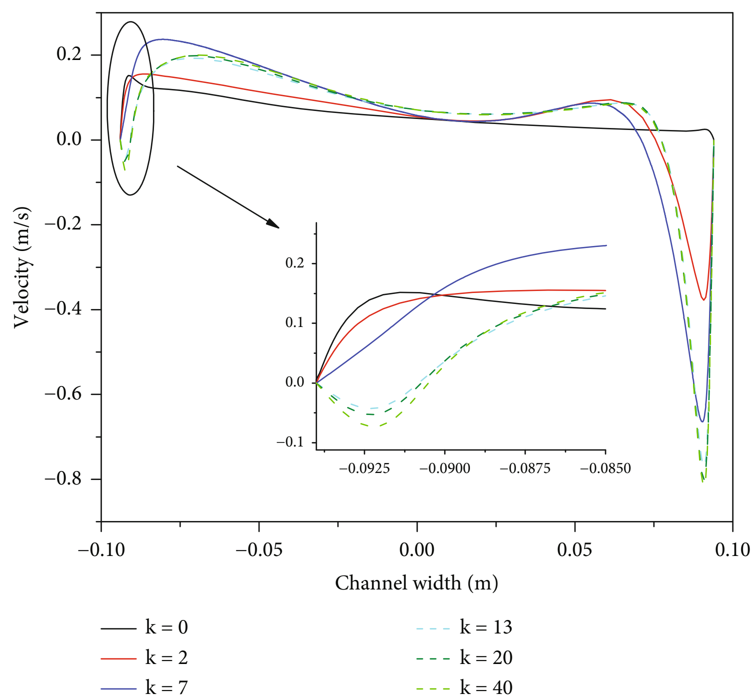

(a)

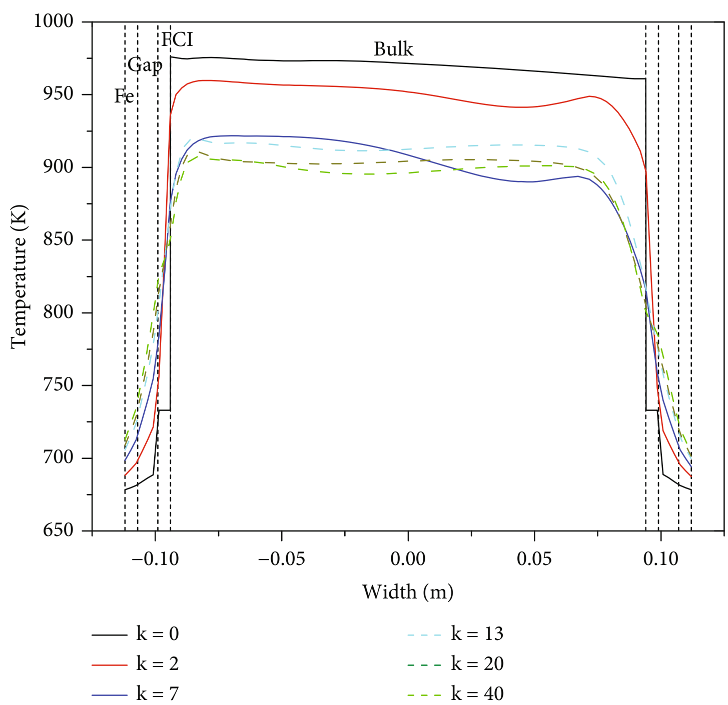

(b)

FIGURE 14: (a) Velocity profile at the outlet of the bulk region and reverse flows occur near the hot wall in unsteady cases. (b) Temperature profile at the outlet with different FCI's thermal conductivity. Steady cases are shown in solid lines, unsteady cases are shown in dash lines, and the bulk flow is unsteady when $\kappa_{FCI} \geq 13\,W/(m \cdot K)$ and $B = 4\,T$.

($B = 1.5\,T$, $Ha = 4800$), and 12.8% ($B = 1.7\,T$, $Ha = 5440$). The phenomenon and mechanism of the fluctuation of pressure drop are analyzed in this part, and interactions among pressure drop, reverse flow, and Lorentz force are concluded.

The process and mechanism of quasiperiodic unsteady flow are analyzed from the perspective of the temperature field. When reverse flow moves to the top, due to the exponential heat source in the chamber, the fluid near the hot wall is accelerated by buoyancy, meanwhile, the fluid near the cold wall is squeezed to flow down so as to keep flow flux conservation. The reverse flow which contains high-temperature fluid falls down. During the process of falling down, the heat contained in reverse flow diffuses out and makes the temperature of fluid near the cold wall higher, which causes the temperature distribution between the hot wall and the cold wall to be more uniform. When the temperature difference is reduced to a small critical value, the kinetic energy of upward motion dominates, and the reverse flow reaches the bottom and is ready to rise up again. During rising up, the temperature difference is increased by a heat source, and the buoyancy effect is gradually enhanced. The increasing buoyancy leads to an increase in the maximum velocity of reverse flow (shown in Figure 9(a)). When the temperature difference increases to a large critical value, the structure of reverse flow is broken by the large buoyancy, which results in the sudden reduction of pressure drop.

To figure out the effects of heat source on flow instability in the blanket, a series of cases with four different heat sources ($Gr_Q = 3.5 \times 10^{10}$, 1.1×10^{11}, 3.5×10^{11}, and 1.1×10^{12}) under different magnetic fields ($B = 0.7 \sim 6$ T) are simulated. In order to make computations feasible, the meshes applied in other cases ($Gr_Q = 3.5 \times 10^{10}$, 1.1×10^{11}, and 1.1×10^{12}) have been reduced to coarse meshes ($105 \times 136 \times 80$) in comparison to the case with $Gr_Q = 3.5 \times 10^{11}$. A phase map about unsteady and steady flow considering the magnetic field and the heat source is built (shown in Figure 11), in which the borderline is expressed by the formula $Ha = 1630 \times (1.12 \times e^{Gr_Q/(4.08\times10^{11})} + 1)$. In the range of $Gr_Q = 3.5 \times 10^{10} \sim 3.5 \times 10^{11}$, flow is steady under a moderate magnetic field ($B < 2$ T). However, as a result of the large buoyancy caused by the large heat source, flow with $Gr_Q = 1.1 \times 10^{12}$ cannot remain steady even under a strong magnetic field (shown in Figure 12(a)). Due to the suppression of the magnetic field, the amplitude of the unsteady flow becomes smaller, and frequency increases. In the case of $Gr_Q = 1.1 \times 10^{12}$, outlet temperature of the bulk region would reach ~1400 K (shown in Figure 12(b)) and is much higher than ~950 K of the case with $Gr_Q = 3.5 \times 10^{11}$.

Viscous friction in the narrow gap regions between walls [42] has a strong suppressing effect on the flow instability. As local Reynolds numbers in the gap region are relatively small and the gap region has a narrow width, the instabilities would be suppressed under general magnetic field and heat source conditions. However, the point signals in Figure 13 show that the fluid flow in the gap region under a weak magnetic field has a slight fluctuation. The fluctuation of temperature in the gap region is caused by the quasiperiod fluctuation of temperature in the bulk region. While the fluctuation of the bulk region is suppressed by a strong magnetic field, such as $B = 4$ T, the flow in the gap region also remains steady. The velocity and temperature time series after 100 seconds of Figure 13 were subjected to FFT analysis. The peak frequencies corresponding to $B = 0.7$ T, $B = 1.5$ T, and $B = 4$ T were found to be 0.01342, 0.00763, and 0, respectively. With the increasing B, the flow instability progressively reduced, leading to a gradual decrease in the peak frequency. Upon reaching $B = 4$ T, the flow achieved stability, indicated by a peak frequency of 0.

The physical mechanism of unsteady flow affected by reverse flow, pressure drop, and Lorentz force is investigated

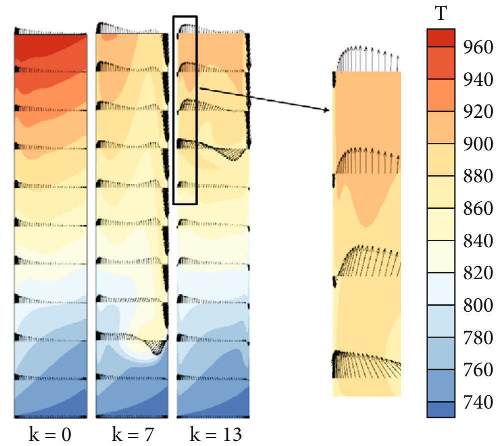

Figure 15: Convection structure with different thermal conductivity of the FCI. A reverse flow occurs near both hot and cold walls at $\kappa_{\mathrm{FCI}} = 13$ W/(m · K) and $B = 4$ T ($Ha = 12800$).

in this section. Due to the large neutron heat source, the temperature difference between the hot wall and cold wall increases and reverse flow occurs. The breakdown of the reverse flow vortex would cause a sudden decrease in pressure drop. Under a weak magnetic field, the fluid flow loses stability and exhibits a quasiperiod fluctuation. The instability of fluid flow in the bulk region cannot be suppressed by a small Lorentz force. When the external magnetic field is strong enough, Lorentz force has a stabilizing effect on flow, the fluctuation of flow disappears, and the flow returns to a steady state.

4.3. Effects of the FCI's Thermal Conductivity. SiC_f/SiC is a candidate material for FCI. SiC/SiC material has weak thermal conductivity, although it is supposed to be thermally insulated. In this section, six cases at FCI's thermal conductivity to be 0, 2, 7, 13, 20, and 40 W/(m·K) are designed to analyze the effects of FCI's thermal conductivity on MHD flow and heat transfer. In all of these cases, the electrical conductivity of the FCI is fixed to 20 S/m. The magnetic field in all of the cases for this analysis is $B = 4$ T. Other parameters, such as $T_{\mathrm{He}} = 673$ K and $Q_0 = 3 \times 10^7$ J/(m^3 · s), are set to be the same as in Section 4.2.

The effects of the FCI's thermal conductivity on velocity and temperature are shown in Figure 14. While $\kappa_{\mathrm{FCI}} = 0$ W/(m · K), the velocity near the hot wall is accelerated by buoyancy. While $\kappa_{\mathrm{FCI}} = 2$ W/(m · K), the cold helium gas begins to cool the fluid in the bulk region, the local Grashof number is increased, and a reverse flow appears near the cold wall. While $\kappa_{\mathrm{FCI}} = 7$ W/(m · K), the effects of the cold helium gas on the bulk region increase, and the velocity of the reverse flow is increased. While $\kappa_{\mathrm{FCI}} = 13$ W/(m · K), the cold helium gas greatly impacts the bulk region, the MHD flow loses stability, and the vortex of reverse flow is broken down. Besides, due to the strong cooling effects of helium gas, reverse flow occurs not only near the cold wall but also near the hot wall. While $\kappa_{\mathrm{FCI}} = 20$ and 40 W/(m·K), the fluid instability is enhanced. The temperature distribution shows that with the increase of FCI's thermal conductivity, the mean

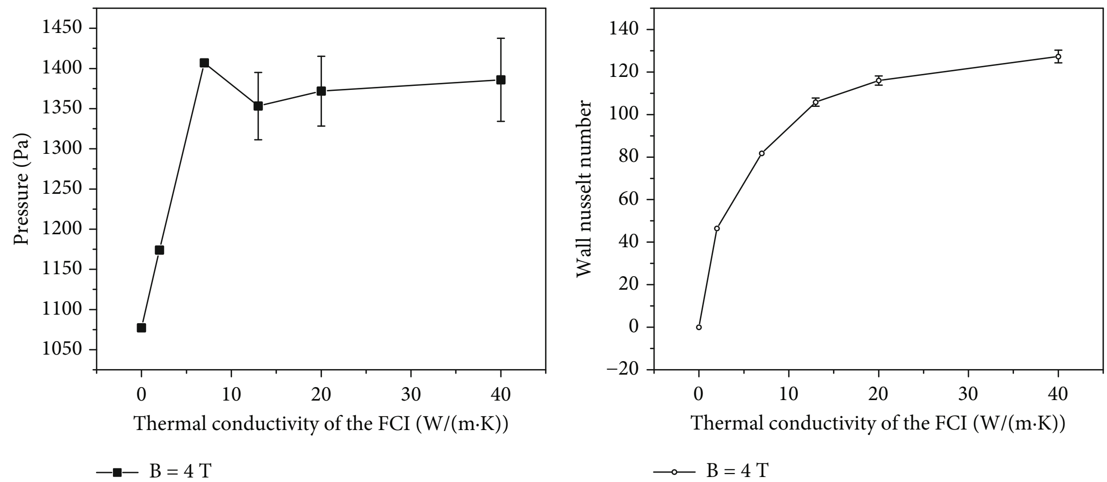

(a) Pressure drop (b) Wall Nusselt number

Figure 16: (a) Pressure drop and (b) wall Nusselt number with different FCI's thermal conductivity when $B = 4\,\mathrm{T}$.

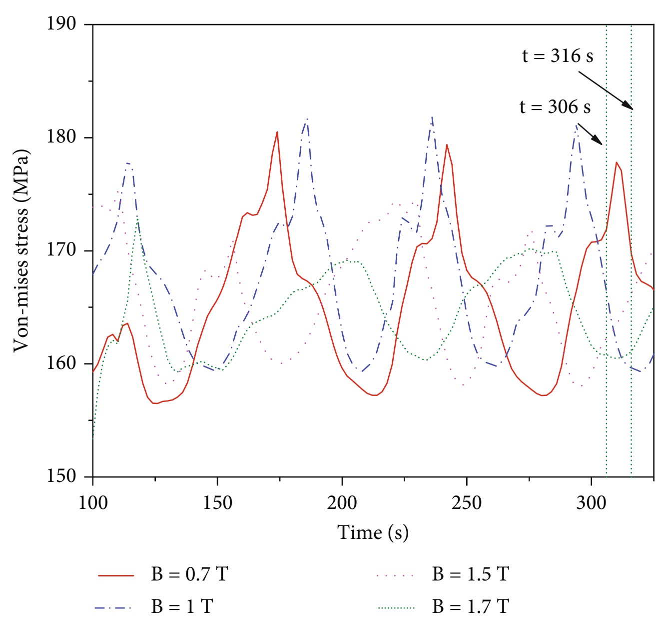

Figure 17: Maximum Von-Mises stress of Hartmann wall of FCI under different magnetic fields change over time at $\kappa_{\mathrm{FCI}} = 2\,\mathrm{W/(m \cdot K)}$.

temperature of the bulk region reduces, and the temperature difference between the inner and outer surfaces of FCI and the temperature of the gap region and Fe wall increase for the heat leakage from the bulk region.

The dynamical processes of the convection structure demonstrated in Figure 15 display the effects of the FCI's thermal conductivity more clearly. The thermal insulated FCI prevents heat leakage from the bulk region to the gap region, and the heat convection and conduction result in the temperature of the bulk region reaching a very high degree of uniformity (as shown in Figure 14(b)). So the local *Gr* and buoyancy are extremely small, and the velocity of the fluid changes only a little. With the κ_{FCI} increasing, the heat transfer between fluid and helium gas is enhanced, which means that helium cooling plays a key role in the instability. As a result, the reverse flow only occurs near the cold wall side at low κ_{FCI} ($\kappa_{\mathrm{FCI}} \leq 7\,\mathrm{W/(m \cdot K)}$), but occurs near both the cold and hot wall at high κ_{FCI} ($\kappa_{\mathrm{FCI}} \geq 13\,\mathrm{W/(m \cdot K)}$). The convective structures with different κ_{FCI} are exhibited in Figure 15. The importance of FCI's thermal conductivity κ_{FCI} to the instability and the special structure of flow in the bulk region are first found and recognized.

The pressure drop is an important issue for the working performance of the blanket. Although FCI is designed as a good thermal and electrical insulator, the thermal conductivity of the FCI mostly ranges from 2 to 20 W/(m·K) [5, 31]. The effect of κ_{FCI} on pressure drop and wall Nusselt number is shown in Figure 16. Due to the buoyant effect, higher thermal conductivity leads to pressure drop increasing for steady flow, while mean pressure drop and amplitude slightly increase for unsteady flow. Wall Nusselt number is enhanced with increasing κ_{FCI}, which is in agreement with

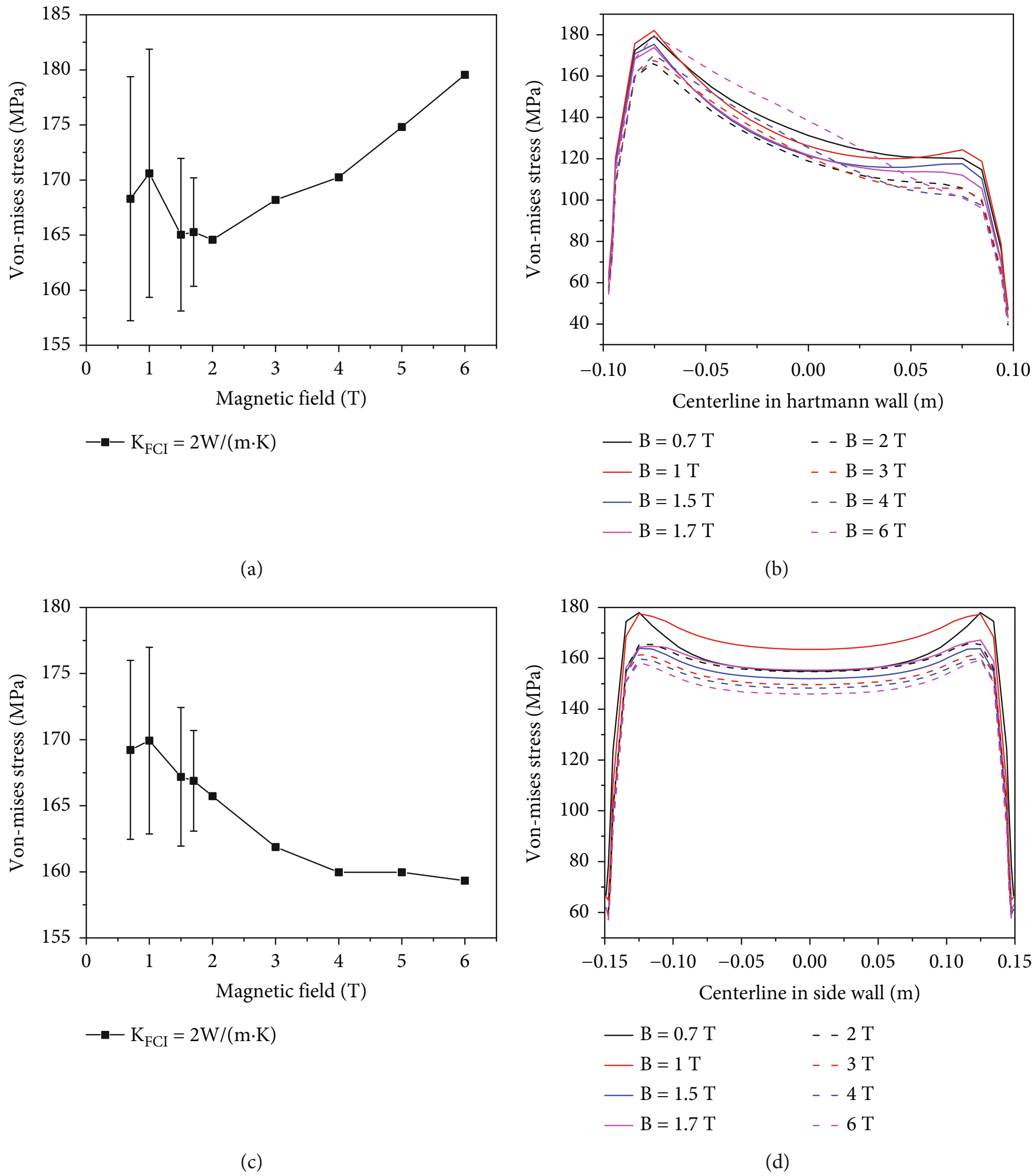

Figure 18: Von-Mises stress of Hartmann and side walls of FCI under different magnetic fields, $\kappa_{FCI} = 2\,\mathrm{W/(m \cdot K)}$. (a) Variation of maximum stress in Hartmann wall in several quasiperiods. (b) The maximum stress profile along the centerline in the Hartmann wall. (c) Variation of maximum stress in the side wall. (d) The maximum stress profile along the centerline in the side wall.

the temperature variation in Figure 14(b). The result of Figure 16(b) shows that the effect of FCI's thermal conductivity has a significant impact on heat transfer efficiency and the instability of fluid flow in a blanket under the same magnetic field ($B = 4\,\mathrm{T}$). The effects of thermal conductivity on pressure drop and heat transfer are also nonlinear and nonmonotonous. The FCI thermal conductivity could be affected by radiation damage, and according to the results of [43, 44], the thermal conductivity of FCI is reduced by radiation damage, and prolonged radiation damage does not cause instability in the bulk region.

4.4. Dynamical Behaviors of FCI. In the above discussion of unsteady flow, fluctuation of the flow field would cause fluctuations of pressure and temperature, which will lead to deformation and vibration of FCI. Figure 17 demonstrates the signals of maximum stress along the outlet centerline in FCI's top Hartmann wall under different magnetic fields. Large amplitude fluctuation of Von-Mises stress, which is caused by the temperature fluctuation of the bulk region, is found. The breakdown of the reverse flow vortex ($B = 0.7\,\mathrm{T}$, $Ha = 2240$, and $t = 306 \sim 316\,\mathrm{s}$) also results in sudden increases of stress, just like the wall Nusselt number.

In Figures 18(a) and 18(c), the FCI's maximum stresses in Hartmann and side walls of unsteady flow cases are generally suppressed by enhancing the magnetic field. When fluid flow is unsteady, the fluctuation of the temperature field would be suppressed with the enhancement of the magnetic field, and the temperature difference across the FCI, as well as the thermal stress, reduces. Stresses in the Hartmann

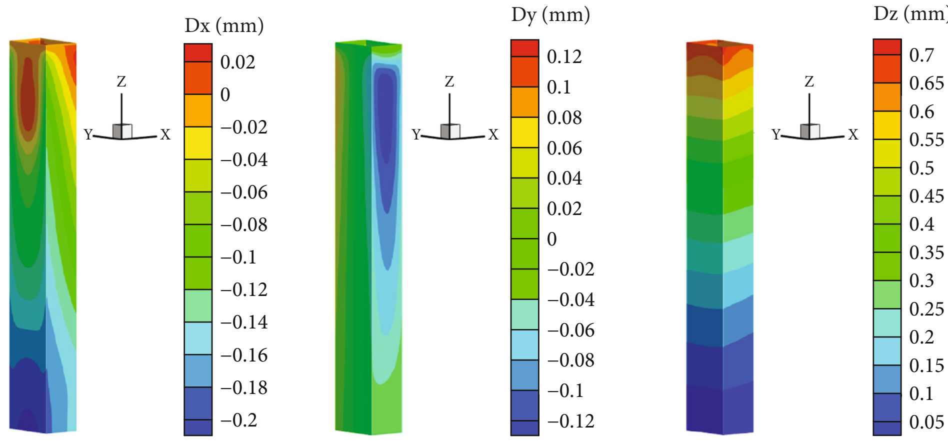

Figure 19: 3D view of displacement in x, y, and z direction when stress in Hartmann wall reaches the maximum value ($t = 310\,\mathrm{s}$) at $\kappa_{\mathrm{FCI}} = 2\,\mathrm{W/(m \cdot K)}$ and $B = 0.7\,\mathrm{T}$ ($Ha = 2240$).

wall of steady flow cases are increased by enhancing the magnetic field, while stresses in the side wall show the opposite trend, which implies an an-isotropic effect of the magnetic field to the temperature field. The computational results display that the left wall (side wall with a large heat source value) has a greater stress than the other three walls. The maximum stress profiles of the top wall and left wall are extracted and shown in Figures 18(b) and 18(d). In the Hartmann wall, the stress distribution is asymmetrical, and stress near a large heat source is higher than stress near a small heat source. The points with the maximum stress are located in the Hartmann wall, and the side wall is safer than the Hartmann wall. Due to the approximate symmetry of the temperature distribution, the stress distribution in the side wall is also approximately symmetric.

Three-dimensional views of FCI's displacements of x, y, and z direction when Mises stress in Hartmann wall $B = 1\,\mathrm{T}$ reaches the maximum value ($B = 0.7\,\mathrm{T}$ and $t = 310\,\mathrm{s}$) are shown in Figure 19. Side walls concave inward along the x direction (radial), while Hartmann wall expands outward along the y direction (toroidal). FCI is elongated along the z direction (poloidal). The other unsteady cases show similar characteristics of deformation.

In conclusion, the unsteady flow would result in quasiperiodic stress in FCI. Besides, the fluctuations of stress and deformation of FCI may lead to structural fatigue failure. The danger from unsteady flow cannot be ignored for structural safety.

5. Conclusions

In this work, a magneto-convective code is used to simulate MHD flow and heat transfer in the DCLL blanket with complex channels under a strong magnetic field and a large heat source. It is found that an unsteady MHD flow would occur with a high Re (31000) and high Gr (3.5×10^{11}) under a moderate magnetic field (0.7~1.7 T), or with a large heat conductivity of FCI. The unsteady flows show large amplitude, low frequency, and quasiperiodic characteristics, rather than the chaos of turbulence. Effects of the unsteady flow on heat transfer and FCI's dynamic behaviors are analyzed in detail. The most important results can be concluded as follows:

(1) The significance of cold helium gas to the instability of fluid flow in the bulk region is discovered and recognized for the first time. Even though Gr_{He} is relatively small compared to Gr_Q, helium gas still plays an important role in the flow characteristics within the bulk region

(2) The importance of the thermal conductance of the FCI to convective structure and instability is revealed. With a moderate thermal conductivity of FCI, an unsteady flow and a reverse flow would occur even under a strong magnetic field

(3) The fluctuations in pressure drop and wall Nusselt number can result from unsteady bulk flow region

(4) Mean Nusselt numbers of unsteady flow and steady flow and the nondimensional pressure drop of steady flow show relationships with the Ha numbers when Gr_Q is fixed, respectively: $Nu_{\mathrm{mean}} = -2.32 \times 10^{-4} \cdot Ha + 49.42$ and $P = 31e^{6.3\times10^{-5}Ha} - 35$

(5) Temperature fluctuations in the bulk region give rise to slightly unsteady flow in the gap region, resulting in temperature and stress fluctuations of the FCI exhibiting quasiperiodic characteristics

(6) Considering the effects of the magnetic field and heat source, a phase diagram has been developed that distinguishes between nonsteady and steady flow. The borderline is expressed by the formula $Ha = 1630 \times \left(1.12 \times e^{Gr_Q/(4.08\times10^{11})} + 1\right)$

The current research has certain limitations, primarily stemming from the parameter range being smaller than the actual magnetic field strength of the blanket. This study is aimed at investigating the problems of MHD flow and heat transfer in a DCLL blanket with complex channels under intense magnetic fields and high heat sources, which display a nonlinear and nonmonotonic relationship with the magnetic field. Due to computational constraints, our current research is limited to a maximum magnetic field strength of 6 T. In real fusion reactor environments, the magnetic field can reach a maximum of 8 T. We have not yet demonstrated the applicability of our conclusions for issues beyond the 6 T range.

Moreover, future research needs to take into account the presence of tritium within the blanket. In addition to the influence of thermal buoyancy, the impact of tritium-induced concentration buoyancy on the flow must also be considered. Currently, the distribution of tritium in the blanket remains unclear, and this aspect will be further investigated. Additionally, if computational capabilities permit, we will explore the effects of higher magnetic field strengths.

Nomenclatures

a: Half radial length of bulk region (m)
b: Half toroidal length of bulk region (m)
$\vec{B}$: Magnetic field (T)
E: Elastic modulus (Pa)
C_p: Specific heat of the fluid (J/(kg·K))
g: Gravitational acceleration (m/s^2)
G: Shear modulus (Pa)
Gr: Grashof number
Gr_{He}: Grashof number of helium gas
Gr_{loc}: Local Grashof number
Gr_Q: Grashof number of heat source
Ha: Hartmann number
$\vec{j}$: Induced current density
Nu: Local Nusselt number
Nu_{mean}: Mean Nusselt number
Nu_s: Streamwise Nusselt number
Nu_w: Wall Nusselt number
p: Pressure (Pa)
P: Ratio of pressure to density p/ρ (Pa·m^3/kg)
Pr: Prandtl number
Q: Internal heat source (J/(m^3·s))
$\bar{Q}$: Average value of heat source Q (J/(m^3·s))
Q_0: Maximum volumetric heat source value (J/(m^3·s))
Re: Reynolds number
T: Temperature of fluid field (K)
T_0: Inlet temperature of fluid (K)
T_{He}: Temperature of helium gas (K)
T_{mean}: Mean temperature (K)
u, v, w: Velocities in x, y, and z directions (m/s)
U: Inlet velocity of fluid (m/s)
U_{mean}: Mean velocity (m/s)
x, y, z: Coordinate system.

Greek Symbols

α: Thermal expansion coefficient of FCI (K^{-1})
β: Coefficient of volumetric expansion (K^{-1})
θ: Nondimensional temperature
κ: Thermal conductivity (W/(m·K))
λ: Lame constant
μ: Dynamic viscosity of the fluid (N·s/m^2)
μ': Poisson's ratio
ν: Kinematic viscosity of fluid (m^2/s)
ρ_0: Density of fluid (kg/m^3)
σ: Electrical conductivity of fluid (S/m)
φ: The electric potential.

Acronyms

fluid: The part of fluid
FCI: The part of FCI
max: Maximum value
min: Minimum value
s: Steady flow
solid: The part of solid
uns: Unsteady flow.

Data Availability

The modeling of DCLL blanket data used to support the findings of this study is included within the article and my previous paper (https://www.sciencedirect.com/science/article/abs/pii/S0017931018338481).

Conflicts of Interest

The authors declare that they have no conflicts of interest.

Acknowledgments

The authors gratefully acknowledge the support from the NSFC (Natural Science Foundation of China) under grant #52176089 and #U23B20110.

References

[1] M. Abdou, D. Sze, C. Wong et al., "U.S. plans and strategy for ITER blanket testing," *Fusion Science and Technology*, vol. 47, no. 3, pp. 475–487, 2005.

[2] S. Smolentsev, R. Moreau, and M. Abdou, "Characterization of key magnetohydrodynamic phenomena in PbLi flows for the US DCLL blanket," *Fusion Engineering and Design*, vol. 83, no. 5-6, pp. 771–783, 2008.

[3] M. Abdou, N. B. Morley, S. Smolentsev et al., "Blanket/first wall challenges and required R&D on the pathway to DEMO," *Fusion Engineering and Design*, vol. 100, pp. 2–43, 2015.

[4] S. Smolentsev, N. Morley, and M. Abdou, "Magnetohydrodynamic and thermal issues of the SiCf/SiC flow channel insert," *Fusion Science and Technology*, vol. 50, no. 1, pp. 107–119, 2006.

[5] S. Smolentsev, N. B. Morley, C. Wong, and M. Abdou, "MHD and heat transfer considerations for the US DCLL blanket for DEMO and ITER TBM," *Fusion Engineering and Design*, vol. 83, no. 10-12, pp. 1788–1791, 2008.

[6] L. Chen, M. Li, M. Ni, and N. Zhang, "MHD effects and heat transfer analysis in magneto-thermo-fluid-structure coupled field in DCLL blanket," *International Communications in Heat and Mass Transfer*, vol. 84, pp. 110–120, 2017.

[7] Z. H. Liu, L. Chen, M. J. Ni, and N. M. Zhang, "Effects of magnetohydrodynamic mixed convection on fluid flow and structural stresses in the DCLL blanket," *International Journal of Heat and Mass Transfer*, vol. 135, pp. 847–859, 2019.

[8] N. Vetcha, S. Smolentsev, M. Abdou, and R. Moreau, "Study of instabilities and quasi-two-dimensional turbulence

in volumetrically heated magnetohydrodynamic flows in a vertical rectangular duct," *Physics of Fluids*, vol. 25, no. 2, article 024102, 2013.

[9] P. Rana, B. Mahanthesh, K. S. Nisar, K. Swain, and M. Devi, "Boundary layer flow of magneto-nanomicropolar liquid over an exponentially elongated porous plate with Joule heating and viscous heating: a numerical study," *Arabian Journal for Science and Engineering*, vol. 46, no. 12, pp. 12405–12415, 2021.

[10] K. Swain, I. L. Animasaun, and S. M. Ibrahim, "Influence of exponential space-based heat source and Joule heating on nanofluid flow over an elongating/shrinking sheet with an inclined magnetic field," *International Journal of Ambient Energy*, vol. 43, no. 1, pp. 4045–4057, 2022.

[11] B. Mahanthesh, W. Al-Kouz, K. Swain, and P. K. Rout, "Computational modeling of heat transfer in magneto-non-Newtonian material in a circular tube with viscous and Joule heating," *Heat Transfer*, vol. 50, no. 7, pp. 6703–6718, 2021.

[12] W. Al-Kouz, K. Swain, B. Mahanthesh, and W. Jamshed, "Significance of exponential space-based heat source and inclined magnetic field on heat transfer of hybrid nanoliquid with homogeneous–heterogeneous chemical reactions," *Heat Transfer*, vol. 50, no. 4, pp. 4086–4102, 2021.

[13] L. Liu and O. Zikanov, "Elevator mode convection in flows with strong magnetic fields," *Physics of Fluids*, vol. 27, no. 4, article 044103, 2015.

[14] O. Zikanov and Y. Listratov, "Numerical investigation of MHD heat transfer in a vertical round tube affected by transverse magnetic field," *Fusion Engineering and Design*, vol. 113, pp. 151–161, 2016.

[15] I. Melnikov, E. Sviridov, V. Sviridov, and N. Razuvanov, "Experimental investigation of MHD heat transfer in a vertical round tube affected by transverse magnetic field," *Fusion Engineering and Design*, vol. 112, pp. 505–512, 2016.

[16] I. Kirillov, D. Obukhov, L. Genin et al., "Buoyancy effects in vertical rectangular duct with coplanar magnetic field and single sided heat load," *Fusion Engineering and Design*, vol. 104, pp. 1–8, 2016.

[17] G. Batchelor and J. Nitsche, "Instability of stationary unbounded stratified fluid," *Journal of Fluid Mechanics*, vol. 227, pp. 357–391, 1991.

[18] L. Y. C. FuWS, Y. Huang, and K. L. Liu, "An investigation of flow reversal of mixed convection in a three dimensional rectangular channel with a finite length," *International Journal of Heat and Mass Transfer*, vol. 64, pp. 636–646, 2013.

[19] C. Gau, K. Yih, and W. Aung, "Reversed flow structure and heat transfer measurements for buoyancy-assisted convection in a heated vertical duct," *Journal of Heat Transfer*, vol. 114, no. 4, pp. 928–935, 1992.

[20] D. Ospir, C. Popa, C. Chereches, G. Polidori, and S. Fohanno, "Flow visualization of natural convection in a vertical channel with asymmetric heating," *International Communications in Heat and Mass Transfer*, vol. 39, no. 4, pp. 486–493, 2012.

[21] X. Zhang and O. Zikanov, "Convection instability in a downward flow in a vertical duct with strong transverse magnetic field," *Physics of Fluids*, vol. 30, no. 11, article 117101, 2018.

[22] U. Burr, L. Barleon, U. Müller, and A. Tsinober, "Turbulent transport of momentum and heat in magnetohydrodynamic rectangular duct flow with strong sidewall jets," *Journal of Fluid Mechanics*, vol. 406, pp. 247–279, 2000.

[23] S. Arcidiacono, I. Di Piazza, and M. Ciofalo, "Low-Prandtl number natural convection in volumetrically heated rectangular enclosures," *International Journal of Heat and Mass Transfer*, vol. 44, no. 3, pp. 537–550, 2001.

[24] R. Khanal and C. Lei, "Flow reversal effects on buoyancy induced air flow in a solar chimney," *Solar Energy*, vol. 86, no. 9, pp. 2783–2794, 2012.

[25] R. Akhmedagaev, O. Zikanov, I. Belyaev, and Y. Listratov, "Magnetoconvection in a horizontal duct flow—a parametric study," *International Journal of Thermal Sciences*, vol. 194, article 108576, 2023.

[26] M. J. Li, J. H. Pan, M. J. Ni, and N. M. Zhang, "Heat transfer and thermal stress analysis in fluid-structure coupled field," *Applied Thermal Engineering*, vol. 88, pp. 473–479, 2015.

[27] S. Ali, C. Habchi, S. Menanteau, T. Lemenand, and J. L. Harion, "Heat transfer and mixing enhancement by free elastic flaps oscillation," *International Journal of Heat and Mass Transfer*, vol. 85, pp. 250–264, 2015.

[28] A. Brēķis, I. Krastiņš, B. P. Polo et al., "Hydrodynamics and electrical insulation of PbLi flow with SiC flow channel inserts in a strong magnetic field," *Fusion Engineering and Design*, vol. 194, article 113920, 2023.

[29] B. Schulz, "Thermophysical properties of the Li (17) Pb (83) alloy," *Fusion Engineering and Design*, vol. 14, no. 3-4, pp. 199–205, 1991.

[30] E. M. De Les Valls, L. Sedano, L. Batet et al., "Lead–lithium eutectic material database for nuclear fusion technology," *Journal of Nuclear Materials*, vol. 376, no. 3, pp. 353–357, 2008.

[31] S. Smolentsev, M. Abdou, N. Morley, M. Sawan, S. Malang, and C. Wong, "Numerical analysis of MHD flow and heat transfer in a poloidal channel of the DCLL blanket with a SiCf/SiC flow channel insert," *Fusion Engineering and Design*, vol. 81, no. 1-7, pp. 549–553, 2006.

[32] M. J. Ni, R. Munipalli, N. B. Morley, P. Huang, and M. A. Abdou, "A current density conservative scheme for incompressible MHD flows at a low magnetic Reynolds number. Part I: on a rectangular collocated grid system," *Journal of Computational Physics*, vol. 227, no. 1, pp. 174–204, 2007.

[33] M. J. Ni, R. Munipalli, P. Huang, N. B. Morley, and M. A. Abdou, "A current density conservative scheme for incompressible MHD flows at a low magnetic Reynolds number. Part II: on an arbitrary collocated mesh," *Journal of Computational Physics*, vol. 227, no. 1, pp. 205–228, 2007.

[34] X. Zhang and O. Zikanov, "Two-dimensional turbulent convection in a toroidal duct of a liquid metal blanket of a fusion reactor," *Journal of Fluid Mechanics*, vol. 779, pp. 36–52, 2015.

[35] I. Orlanski, "A simple boundary condition for unbounded hyperbolic flows," *Journal of Computational Physics*, vol. 21, no. 3, pp. 251–269, 1976.

[36] A. Dezfulizadeh, A. Aghaei, and G. A. Sheikhzadeh, "Comprehensive 3E analyses of a parabolic trough collector equipped with an innovative combined twisted turbulator," *Engineering Analysis with Boundary Elements*, vol. 150, pp. 507–527, 2023.

[37] A. R. M. Dovom, A. Aghaei, A. H. Joshaghani, A. Dezfulizadeh, and A. Kakavandi, "Numerical analysis of heating aerosol carbon nanofluid flow in a power plant recupesrator with considering ash fouling: a deep learning approach," *Engineering Analysis with Boundary Elements*, vol. 141, pp. 75–90, 2022.

[38] Y. Zheng, S. Yaghoubi, A. Dezfulizadeh, S. Aghakhani, and I. Tlili, "Free convection/radiation and entropy generation analyses for nanofluid of inclined square enclosure with

uniform magnetic field," *Journal of Thermal Analysis and Calorimetry*, vol. 141, no. 1, pp. 635–648, 2020.

[39] A. Dezfulizadeh, A. Aghaei, A. H. Joshaghani, and M. M. Najafizadeh, "Exergy efficiency of a novel heat exchanger under MHD effects filled with water-based Cu–SiO 2-MWCNT ternary hybrid nanofluid based on empirical data," *Journal of Thermal Analysis and Calorimetry*, vol. 147, no. 7, pp. 4781–4804, 2022.

[40] P. Norajitra, L. Bühler, U. Fischer, S. Malang, G. Reimann, and H. Schnauder, "The EU advanced dual coolant blanket concept," *Fusion Engineering and Design*, vol. 61-62, pp. 449–453, 2002.

[41] S. Smolentsev, N. Morley, and M. Abdou, "Code development for analysis of MHD pressure drop reduction in a liquid metal blanket using insulation technique based on a fully developed flow model," *Fusion Engineering and Design*, vol. 73, no. 1, pp. 83–93, 2005.

[42] L. E. Schmidt, E. Calzavarini, D. Lohse, F. Toschi, and R. Verzicco, "Axially homogeneous Rayleigh–Bénard convection in a cylindrical cell," *Journal of Fluid Mechanics*, vol. 691, pp. 52–68, 2012.

[43] M. Rohde, "Reduction of the thermal conductivity of SiC by radiation damage," *Journal of Nuclear Materials*, vol. 182, pp. 87–92, 1991.

[44] D. Senor, D. Trimble, G. Youngblood, G. Newsome, C. Moore, and J. Woods, "Effects of neutron irradiation on thermal conductivity of SiC-based composites and monolithic ceramics," *Fusion Technology*, vol. 30, no. 3P2A, pp. 943–955, 1996.